LASER-PROBE ANALYSIS OF MODERN ELECTROACOUSTIC MICROWAVE DEVICES

Doctoral Dissertation

Olli Holmgren

Helsinki University of Technology
Faculty of Information and Natural Sciences
Department of Applied Physics

LASER-PROBE ANALYSIS OF MODERN ELECTROACOUSTIC MICROWAVE DEVICES

Doctoral Dissertation

Olli Holmgren

Helsinki University of Technology
Faculty of Information and Natural Sciences
Department of Applied Physics

Teknillinen korkeakoulu
Informaatio- ja luonnontieteiden tiedekunta
Teknillisen fysiikan laitos

ABSTRACT OF DOCTORAL DISSERTATION	HELSINKI UNIVERSITY OF TECHNOLOGY P.O. BOX 1000, FI-02015 TKK http://www.tkk.fi

Author

Name of the dissertation

Manuscript submitted	Manuscript revised

Date of the defence

Monograph	Article dissertation (summary + original articles)

Faculty
Department
Field of research
Opponent(s)
Supervisor
Instructor

Abstract

Keywords

ISBN (printed)	ISSN (printed)
ISBN (pdf)	ISSN (pdf)
Language	Number of pages

Publisher

Print distribution

The dissertation can be read at http://lib.tkk.fi/Diss/

VÄITÖSKIRJAN TIIVISTELMÄ	TEKNILLINEN KORKEAKOULU PL 1000, 02015 TKK http://www.tkk.fi
Tekijä	

Väitöskirjan nimi	

Käsikirjoituksen päivämäärä	Korjatun käsikirjoituksen päivämäärä

Väitöstilaisuuden ajankohta	
☐ Monografia	☐ Yhdistelmäväitöskirja (yhteenveto + erillisartikkelit)

Tiedekunta
Laitos
Tutkimusala
Vastaväittäjä(t)
Työn valvoja
Työn ohjaaja

Tiivistelmä

Asiasanat

ISBN (painettu)	ISSN (painettu)
ISBN (pdf)	ISSN (pdf)
Kieli	Sivumäärä

Julkaisija
Painetun väitöskirjan jakelu
☐ Luettavissa verkossa osoitteessa http://lib.tkk.fi/Diss/

Preface

List of Publications

This thesis consists of an overview and of the following publications:

I O. Holmgren, J. V. Knuuttila, T. Makkonen, K. Kokkonen, V. P. Plessky, W. Steichen, M. Solal, and M. M. Salomaa, "Imaging surface acoustic fields in a longitudinal leaky wave resonator", *Applied Physics Letters* **86**, 024101 (2005).

II O. Holmgren, T. Makkonen, J. V. Knuuttila, M. Kalo, V. P. Plessky, and W. Steichen, "Side radiation of Rayleigh waves from synchronous SAW resonators", *IEEE Transactions on Ultrasonics, Ferroelectrics, and Frequency Control* **54**(4), pp. 861-869 (2007).

III J. Meltaus, S. S. Hong, O. Holmgren, K. Kokkonen, and V. P. Plessky, "Double-resonance SAW filters", *IEEE Transactions on Ultrasonics, Ferroelectrics, and Frequency Control* **54**(3), pp. 659-667 (2007).

IV M. Solal, O. Holmgren, and K. Kokkonen, "Design, modelling and visualization of R-SPUDT devices with transverse mode suppression", *IEEE Transactions on Ultrasonics, Ferroelectrics, and Frequency Control*, accepted for publication.

V O. Holmgren, K. Kokkonen, T. Mattila, V. Kaajakari, A. Oja, J. Kiihamäki, J. V. Knuuttila, and M. M. Salomaa, "Imaging of in- and out-of-plane vibrations in micromechanical resonator", *Electronics Letters* **43**(3), pp. 16-17 (2005).

VI O. Holmgren, K. Kokkonen, T. Veijola, T. Mattila, V. Kaajakari, A. Oja, J. V. Knuuttila, and M. Kaivola, "Analysis of vibration modes in a micromechanical square-plate resonator", *Journal of Micromechanics and Microengineering* **19**, 015028 (2009).

Throughout the overview, these publications are referred to by their Roman numerals.

Author's contribution

The studies in this dissertation are the result of work carried out in the Materials Physics Laboratory, in the Optics and Molecular Materials Laboratory and in the Department of Applied Physics at Helsinki University of Technology (TKK), Finland, during the years 2003-2008. Publications **I** and **II** were prepared in collaboration with TEMEX, Sophia-Antipolis, France and with Victor P. Plessky (GVR Trade SA, Bevaix, Switzerland). Publication **III** was prepared in collaboration with Seong Su Hong (Samsung Electro-mechanics Co., Ltd., Suwon, Korea) and with Victor P. Plessky. Publication **IV** resulted from a collaboration with Marc Solal, TriQuint Semiconductor, Apopka, Florida, USA. Publications **V** and **VI** were prepared in collaboration with Technical Research Center VTT, Espoo, Finland. Publication **VI** included also collaboration with Timo Veijola (Department of Radio Science and Engineering at TKK, Finland).

The author has substantially contributed to all research presented in Publications **I**–**VI**. He conducted all interferometric measurements presented in Publications **I**–**VI** and was mainly responsible for their planning and data analysis. The detection method for the in-plane vibrations presented in Publications **V** and **VI** was developed by the author, Kimmo Kokkonen and Jouni V. Knuuttila. Publications **I**, **II**, **V** and **VI** were mostly written by the author. The part of Publication **IV** covering the interferometric measurements was mainly written by the author. He also contributed to the writing of the part of Publication **III** involving the interferometric measurements.

Most of the results presented in Publications **I**–**VI** have been presented in the annual IEEE Ultrasonics Symposia: those of Publications **V** and **VI** by the author, those of Publication **III** by J. Meltaus and the author, those of Publication **I** and **II** by T. Makkonen and J. V. Knuuttila, and those of Publication **IV** by M. Solal.

List of abbreviations

The following abbreviations are used in the overview:

AFM	Atomic force microscope
BAW	Bulk acoustic wave
CCD	Charge coupled device
COM	Coupling of modes
CRF	Coupled resonator filter
DART	Distributed array reflection transducer
DLP	Digital light processing
FBAR	Thin film bulk acoustic wave resonator
FEM	Finite element method
IDT	Interdigital transducer
IEF	Impedance element filter
IC	Integrated circuit
LLSAW	Longitudinal leaky surface acoustic wave
LSAW	Leaky surface acoustic wave
MEMS	Microelectromechanical systems
NEMS	Nanoelectromechanical systems
RF	Radio frequency
R-SPUDT	Resonant single-phase unidirectional transducer
SAW	Surface acoustic wave
SE	Square extensional
SEM	Scanning electron microscope
SPUDT	Single-phase unidirectional transducer

Contents

1 Introduction

The increasing functionality of modern mobile phones, along with the demand for small size and light weight, present a challenge for the component design. Surface acoustic wave (SAW) components have proven to be a part of the solution to this challenge. In particular, intermediate frequency and radio frequency (RF) filters employing SAWs have become extensively applied in cellular handsets. A modern mobile phone can contain up to seven SAW filters. The SAW filters feature many advantages compared to components based on competing technologies. They are compact in size, light in weight, and moreover, they are suitable for mass production and hence cost effective. In addition, the performance of SAW filters is excellent, that is, they feature low losses, flat passband, steep skirts, and a high suppression level at the stopband [1]. Traditionally, SAW filters have been utilized, for example, in television receivers and in military applications such as radars and missiles [2].

Recently, increasing interest has also been devoted to microelectromechanical systems (MEMS) to reach high integrability. For example, one bulky component still remaining in modern mobile phone architecture is the quartz reference oscillator. Micromechanical resonators offer an attractive alternative for those oscillators since they possess compact size, integrability with integrated circuit (IC) electronics and excellent performance (e.g., high quality factor, low phase noise and low power consumption).

SAW and MEMS devices have been modeled using various methods, but these are presently not fully matured. The models do not yet satisfactorily explain all the electroacoustic phenomena involved. Thus, imaging the surface vibrations in these devices is important as a means to explore non-explained phenomena, such as unexpected losses in the electrical response, spurious resonances and parasitic vibration modes. Characterization of vibration fields is important as a way to validate the design, operation and performance of the devices. Optical probing is a powerful tool for the task since the vibrations can be studied directly without perturbing the device operation. Furthermore, optical measurements provide direct physical information about the acoustic fields within the electroacoustic devices not obtainable via measuring the electrical response. Hence, the optical measurements directly support the research and development of these devices.

A scanning laser interferometer is one option for the imaging task. Two such instruments with unique characteristics have been constructed at Helsinki University of Technology (TKK). The laser interferometers feature excellent sensitivity and lateral resolution, while automated areal scans ensure precise, accurate and fast imaging of surface vibrations in microacoustic devices.

In this thesis, SAW and MEMS devices are analyzed using the scanning Michelson interferometer at TKK. In Section 2, basics of the laser interferometry is discussed, followed by an overview of the scanning Michelson interferometer developed at TKK. The rest of the thesis is divided into parts: Sections 3 and 4 deal with studies of SAW and MEMS devices, respectively. Background information of SAW devices is presented in Sec. 3.1, followed by an overview of imaging vibrations in such devices (Sec. 3.2). A short overview of different loss mechanisms and transverse waveguide modes in SAW devices is given in Sec. 3.3. Section 3.4 summarizes the main results of the thesis, related to SAW devices. Section 4 begins with an introduction to MEMS and micromechanical resonators. An overview of systems applied to image vibrations in MEMS devices is presented in Sec. 4.2. Section 4.3 represents a novel measurement method for detection and mapping of in-plane vibrations in MEMS resonators. Section 4.4, describes the results and discussion related to a MEMS resonator analyzed in this thesis. Finally, Section 5 concludes the thesis.

2 Laser-interferometry of electroacoustic devices

Optical interferometry has been applied as a laboratory technique for more than a hundred years. Currently, it is suitable for a very wide range of tasks, such as for measuring accurately distances, displacements and vibrations, for testing optical systems and for measuring temperature and pressure [3]. One of the most common configurations of optical interferometry is the Michelson interferometer, invented by Albert Abraham Michelson in the late 19th century [4, 5].

In this work, a scanning Michelson laser interferometer [6] is employed to measure small vibration amplitudes on the surface of SAW and MEMS devices. For this purpose, optical interferometry features several advantages. First, it is non-contacting, and therefore, it does not disturb the vibration field and the measurement point may be quickly moved. Second, a spatial resolution in the lateral direction of less than one micrometer can be obtained, if necessary. Furthermore, high accuracy in determining the vibration amplitude may be achieved since the displacements are compared with the known wavelength of the laser light which is 632.8 nm for the Helium-Neon laser used.

2.1 Operation principle of the Michelson interferometer

A basic setup of the Michelson-type laser interferometer is depicted in Fig. 2.1. A laser is used as the light source, providing monochromatic and coherent light. The laser beam is divided into two parts by a beam splitter. One beam is transmitted to the sample, while the other one is directed to a reference mirror. After being reflected from the targets, both beams are directed by the beam splitter onto a photodetector, where the beams interfere and the optical power is detected.
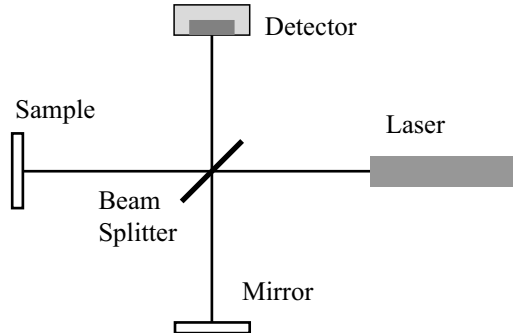
Figure 2.1: Basic Michelson interferometer.

To calculate the optical power at the photodetector, it is assumed that both beams have the same polarization state and that the sample surface is vibrating sinusoidally with an amplitude δ at the frequency $f_s = \omega_S/2\pi$, where ω_s is the angular frequency. The electric fields of the sample and reference beams, with amplitudes A_S and A_R, are

$$
\begin{aligned}
E_S &= A_S \exp\{i\omega_0 t - 2ik_0[L_S + \delta\sin(\omega_S t)]\} \\
E_R &= A_R \exp[i\omega_0 t - 2ik_0(L_R + \Delta)],
\end{aligned}
\tag{2.1}
$$

where ω_0 is the angular frequency of the laser light, $k_0 = \frac{2\pi}{\lambda}$ is the optical wavenumber, λ is the wavelength of the laser, Δ is the displacement of the reference mirror, and L_S and L_R are the optical path lengths of the sample and reference beams, respectively. When the sample and reference beams interfere, the total electric field at the photodetector is the sum of E_S and E_R. Hence, the optical power at the photodetector is

$$
P_{PD} \propto (E_R + E_S)(E_R + E_S)^*,
\tag{2.2}
$$

where the asterisk denotes the complex conjugate. Applying Eqs. (2.1), we obtain

$$
\begin{aligned}
P_{PD} &\propto A_R^2\{1 + R^2 + 2R\cos[2k_0\Delta' + 2k_0\delta\sin(\omega_S t)]\} \\
&\propto A_R^2\{1 + R^2 \quad + 2R\cos(2k_0\Delta')\cos[2k_0\delta\sin(\omega_S t)] \\
&\qquad\qquad - 2R\sin(2k_0\Delta')\sin[2k_0\delta\sin(\omega_S t)]\},
\end{aligned}
\tag{2.3}
$$

where $R = \frac{A_S}{A_R}$ and $\Delta' = \Delta + \frac{L_R - L_S}{2}$ is the total path length difference between the reference and sample beams. For the cosine and sine terms, a Fourier-Bessel expansion may be used [7]

$$
\begin{aligned}
\cos[2k_0\delta\sin(\omega_S t)] &= J_0(2k_0\delta) + 2\sum_{q=1}^{\infty} J_{2q}(2k_0\delta)\cos(2q\omega_S t), \\
\sin[2k_0\delta\sin(\omega_S t)] &= 2\sum_{q=0}^{\infty} J_{2q+1}(2k_0\delta)\sin[(2q+1)\omega_S t],
\end{aligned}
\tag{2.4}
$$

where $J_i, (i = 0, 1, 2, 3, ...)$ are Bessel functions of the first kind and q is a positive integer. Applying these, Eq. (2.3) becomes

$$
\begin{aligned}
P_{PD} &\propto A_R^2\{1 + R^2 + 2R\cos(2k_0\Delta')[J_0(2k_0\delta) + 2J_2(2k_0\delta)\cos(2\omega_S t) + \cdots] \\
&\quad - 2R\sin(2k_0\Delta')[2J_1(2k_0\delta)\sin(\omega_S t) + 2J_3(2k_0\delta)\sin(3\omega_S t) + \cdots]\}.
\end{aligned}
$$

The signal consists of different spectral components: the zeroth order component, and the first, second and higher order harmonics. If we assume that the vibrations are small compared to the wavelength of the laser, that is $2k_0\delta << 1$, the optical power at the photodetector may be approximated by

$$
P_{PD} \propto A_R^2[1 + R^2 + 2R\cos(2k_0\Delta') - 4k_0\delta R\sin(2k_0\Delta')\sin(\omega_S t) + ...],
\tag{2.5}
$$

where we have used $J_0(2k_0\delta) \approx 1$ and $J_1(2k_0\delta) \approx \frac{1}{2}2k_0\delta$. Hence, the phase modulation of the sample beam caused by the vibrating sample surface is transformed into a modulation of the laser power at the photodetector due to the interference of the sample and reference beams. The maximum modulation of the optical power at the photodetector at the angular frequency ω_S occurs when $\sin(2k_0\Delta') = 1$, i.e., the phase difference is $\Delta\phi = 2k_0\Delta' = \frac{\pi}{2} + n\pi$, where n is an integer. These points are called quadrature points.

The optical power at the photodetector is plotted in Fig. 2.2 as a function of the optical phase difference between the two interferometer arms (or the mirror displacement normalized to the laser wavelength). When the position of the reference mirror is adjusted, the operation point of the interferometer moves on the curve. When the operation point coincides with a quadrature point, a vibration of the sample surface causes the largest possible modulation of the optical power at the detector, as illustrated in Fig. 2.2. Furthermore, assuming small vibrations, the response of the interferometer can be assumed to be linear. If the vibration amplitude is $\delta < 30$ nm, $J_1(2k_0\delta)$ differs less than 5 % from the linear term, $k_0\delta$.
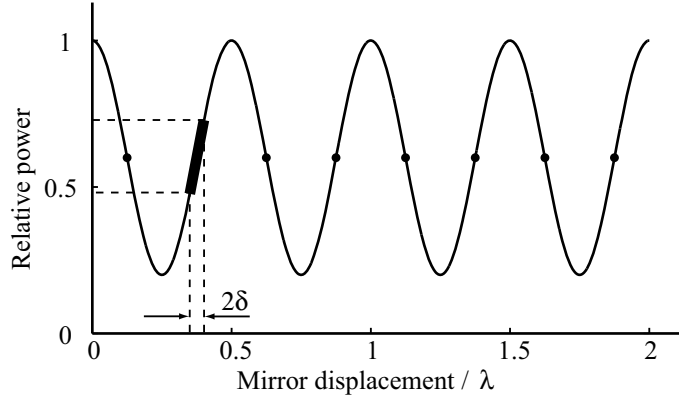
Figure 2.2: Optical power at the photodetector as a function of mirror displacement. At the quadrature points marked with dots, a small surface vibration causes the largest modulation of the detected light power.

2.2 The scanning Michelson interferometer at TKK

The measurements in this thesis were carried out using the scanning laser interferometer constructed by Knuuttila et al. [6, 8, 9]. The first measurements with the probe were performed in 1996. Since then, it has been actively used to measure numerous samples, while at the same time, it has been continuously developed.

Figure 2.3 depicts the setup of the scanning Michelson interferometer. Only a few optical components are added compared to the basic configuration shown in Fig. 2.1. The light source is a linearly polarized TEM$_{00}$-mode He-Ne laser, model Uniphase 1135P ($\lambda = 632.8$ nm, $P = 10$ mW). The polarization plane of the laser is adjusted to be along the vertical plane by rotating the laser. After the beam leaves the laser, it passes through an optical isolator (OFR IO-2-633-LP), where the polarization plane is rotated by 45°. Then the beam is collimated using a microscope objective and a lens. The diameter of the collimated beam is 2.0 mm at the waist.
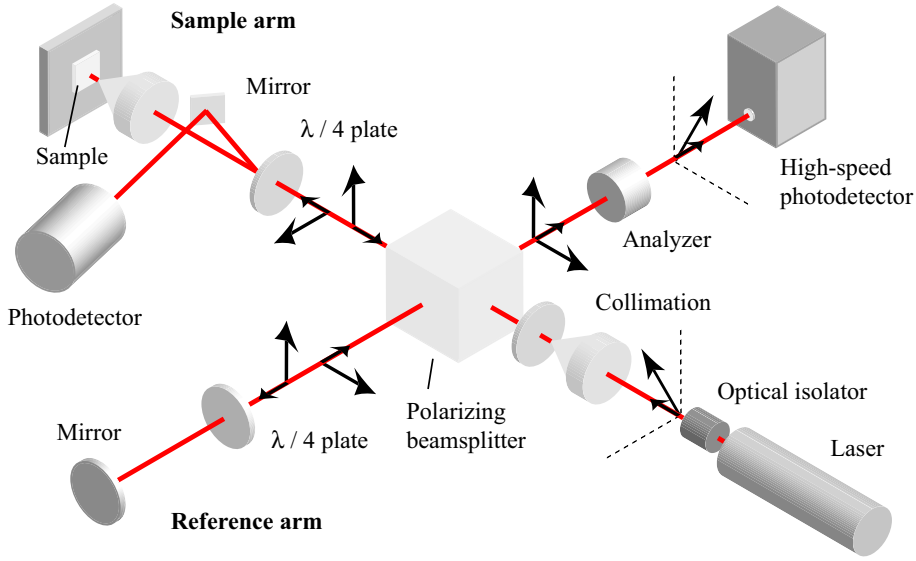
Figure 2.3: Michelson laser interferometer developed at TKK.

A polarizing beam splitter divides the laser beam into a reference and a sample beam such that the reflected beam is vertically polarized whereas the transmitted beam is horizontally polarized. The vertically polarized reference beam propagates through a $\lambda/4$ plate, which transforms it into a right-handed circularly polarized beam. Upon reflection from the reference mirror, the polarization state of the beam is transformed into left-handed circularly polarized. Passing again through the $\lambda/4$ plate, the polarization of the beam is transformed into horizontal polarization. After that, the reference beam passes through the polarizing beam splitter towards an analyzer.

The sample beam is focused onto the sample surface with a microscope objective (Nikon 354248 CF N Plan 40 x ELWD), which has a numerical aperture of 0.55 and working distance of 5.08–6.84 mm. The focused spot size, $2w_0$, is 1.6 μm, which was experimentally determined using a method similar to that reported in [10]. After pass-

ing a second time through the $\lambda/4$ plate, the sample beam is lead to the analyzer through the beam splitter. At the analyzer placed at an angle of 45° relative to the vertical direction, the two orthogonally polarized beams are mixed to interfere on the detector surface. The interference signal is measured with a high-speed silicon photodetector (Newport 818-BB-21). According to the manufacturer, the cut-off frequency of the detector is higher than 400 MHz, after which the sensitivity of the detector begins to decrease. Still, interference signals at frequencies exceeding 2 GHz have been successfully measured [11].

A number of other instruments in addition to the optical components are required to create a complete measurement system. In the detection electronics, a feed-thru terminator of 50 Ω is used to transform the current signal from the high-speed detector into a voltage signal. This signal is then filtered with an RF filter and amplified before the signal is fed into a spectrum analyzer (HP 8694E). The operation frequency range of the spectrum analyzer is 9 kHz – 2.9 GHz, while the receiver bandwidth may be selected in the range 1 kHz – 3 MHz. The spectrum analyzer is also capable of operating in zero-span mode, which enables the signal amplitude to be measured at a selected frequency as a function of time. To provide electrical excitation to the sample, a signal generator (HP 8648D) is used with a frequency range of 9 kHz – 4 GHz and a maximum output power of 21 dBm which corresponds to 126 mW.

As discussed above, the Michelson interferometer must be adjusted to one of its quadrature points to maximize its sensitivity. This is done in the following way in our system: The spectrum analyzer is used in the zero-span mode to measure the signal as a function of time. A trigger signal is sent to the spectrum analyzer to start a sweep while the reference mirror is simultaneously moved at a constant velocity using a piezoelectric transducer. Doing so, the operating point of the interferometer is swept over several quadrature points. The measured signal as a function of time is shown in Fig. 2.4, where each maximum corresponds to one quadrature point. The relative amplitude of the surface vibration is then determined by locating and averaging several maxima. It should be noted that the spectrum analyzer does not provide phase information. For measurement of the phase, stabilization of the laser interferometer would be required. As a matter of fact, it is also possible to measure the phase without stabilization using a sweep of the reference mirror and a vector network analyzer [12], but in such a case, locking into a known quadrature point is extremely important [13]. Absolute amplitude values could be obtained by doing a calibration procedure [6].

The sample is moved under the focus spot utilizing three linear translation stages (Newport MFN25CC) which allow us to carry out accurate areal scans with a minimum incremental step of 55 nm and a range of 25 mm. The finite speed of the translation
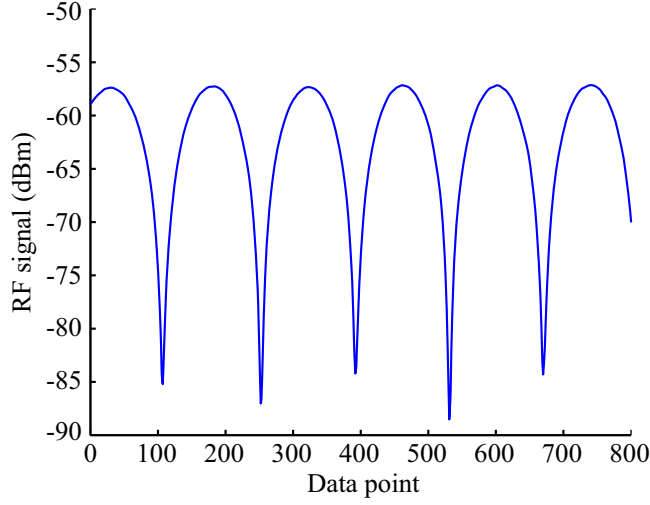
Figure 2.4: Amplitude data from a single sweep of the spectrum analyzer used in the zero-span mode. The RF signal at the frequency f_S is plotted as a function of time, or displacement of the reference mirror.

stages and the sweep time of the reference mirror set a limit to the scanning speed of our laser interferometer. Up to 55 000 points/h may be measured with a small scan step and with an optimized scan area. The minimum detectable vibration amplitude of the interferometer is approximately 0.3 pm for a detection bandwidth of 1 kHz [6].

A photodetector has been added to the sample arm to measure the optical power reflected from the sample. For this purpose, a stray beam reflection from the quarter-wave plate is used (see Fig. 2.3) instead of inserting an additional beam splitter to reflect a part of the sample beam to the photodetector. In this way, the reflectance of the sample surface can be recorded at each measurement point without additional optical losses to the interferometer. By plotting the reflectance data, a micrograph-like image of the scan area, hereafter called light-reflection image, is obtained. With this arrangement, it is easy to compare the position of the acoustic amplitude field with the image of the sample structure point by point.

The scanning laser interferometer is fully automated. The high-precision translation stages, the signal generator, the spectrum analyzer and the multi I/O card are managed by a dedicated control software developed at TKK. Visual Basic was chosen as the programming language back in 1997, mainly because all three interface cards, the motion controller (Newport MM2000), the GPIB (NI AT-GPIB/TNT) and the multi I/O card (NI PCI-MIO-16XE-10), provided full support for Visual Basic including all the necessary drivers and dynamic link libraries.

3 Surface-acoustic-wave devices

3.1 Background

Acoustic waves are propagating deformations of an elastic medium. In a bounded medium, two main groups of acoustic waves exist: bulk acoustic waves (BAW) and surface acoustic waves (SAW). The bulk waves propagate inside the medium, for example, as a plane wave. The surface waves, on the other hand, are confined to the close vicinity of the surface, typically within a distance of one or few wavelengths of the propagating wave. The boundary conditions and the structural and symmetry properties of the material determine the types of acoustic waves propagating in the material. In general, the waves can have displacements in the propagation direction (longitudinal waves) and in the direction perpendicular to the propagation (shear waves, both vertical and horizontal). A common wave mode used in SAW devices is the Rayleigh wave, named after its discoverer, Lord Rayleigh [14]. The displacement components of the Rayleigh wave lie in the xz plane and decay exponentially into the bulk. Here, x and z are parallel to the wave propagation direction and to the surface normal, respectively. The proportion of the x and z components depends on the chosen substrate material. Another common surface acoustic wave is a leaky SAW (LSAW). It is quite similar to the Rayleigh wave, except that it has attenuation or propagation loss because it is coupled to the slow shear BAW.

Usually the materials employed as substrates for SAW devices are electrical insulators that exhibit piezoelectricity. Piezoelectricity is a phenomenon which couples elastic stresses and strains to electric fields and electric displacements in an anisotropic medium. Hence, using piezoelectric materials and proper transducers, electrical signals can be transformed to SAWs and vice versa. The most common materials presently used in SAW devices are quartz (SiO_2), lithium niobate ($LiNbO_3$), and lithium tantalate ($LiTaO_3$).

When designing and fabricating SAW devices, it is essential to specify the orientation and cut of the substrate material exactly. For most crystalline materials, the internal structure is referred to with respect to an orthogonal set of axes denoted by upper-case symbols X, Y, Z with the axis directions defined in relation to the crystal lattice. It is conventional to relate the direction of the surface normal z and the propagation direction x to these axes. Usually, the surface normal direction z is defined first, followed by the propagation direction x [15]. The orientation of z is also referred to as the crystal cut. For example, a YZ-$LiNbO_3$ crystal is Y-cut, and it has the crystal Y-axis parallel to z and the crystal Z-axis parallel to x. Alternatively, the Euler angles (ϕ, θ, ψ) can be used to specify the crystal orientation. Particularly, this notation is ap-

plied with double-rotated cuts that are used when the desired features for the substrate are not achieved with a single-rotated cut defined by the X, Y, Z notation [16]. The first two angles ϕ and θ determine the cut of the substrate, while the angle ψ determines the propagation direction of the SAW. Substrates with a single-rotated cut are preferred in SAW devices since in double-rotated cuts, two angles have to be adjusted in the fabrication process instead of one, rendering the process more prone to errors.

SAW devices may be considered to consist of basic building blocks, such as an interdigital transducer (IDT) and a reflecting grating. The first IDT was realized by White and Voltmer [17] in 1965. This kind of a structure is obtained by depositing metal electrodes on the surface of a piezoelectric substrate, see Fig. 3.1. By applying an AC voltage to the IDT, surface acoustic waves are generated on the substrate. A reflector grating is typically composed of metal stripes or grooves on the surface of the substrate. The reflector is of short-circuit type when all the electrodes are electrically interconnected. The reflector may also be of open-circuit type with electrically isolated fingers, providing different reflectivity in comparison to the short-circuited reflector.
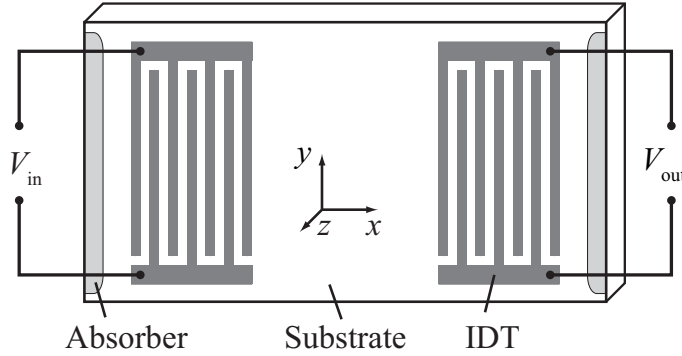
Figure 3.1: Delay line consisting of two IDTs. SAWs propagate along the $+x$ direction from the input to the output IDT.

Figure 3.1 depicts a basic SAW device, a SAW delay line consisting of two IDTs. One IDT is transmitting (in both $\pm x$ directions), whereas the other one is receiving. Absorbers are needed to prevent spurious reflections from the edge of the substrate. Typical time delays are in the range 1–50 μs [18]. The delay line may also be considered as a simple filter architecture. The performance of the delay line filter is excellent in most respects, e.g. it features a highly linear phase response, but the insertion loss is rather high. The structure composed of two IDTs has at least 6 dB of losses. A typical insertion loss of the delay line filter is on the order of 10 dB [18]. Improved performance may be achieved by making modifications to the original IDT structure,

such as in a single-phase unidirectional transducer (SPUDT) [19,20] or in a distributed array reflection transducer (DART) [21]. The SPUDT structure is directive, i.e., it emits SAWs more efficiently into one direction than the opposite direction due to a separation of the transduction and reflection centers within one period of the IDT. In a DART type SPUDT this separation is achieved by using wide reflector electrodes within the period. An extension to the DART structure is the electrode-width-controlled SPUDT [22]. In a resonant SPUDT (R-SPUDT) [23], the transducer contains local resonant cavities while the overall unidirectionality remains.

Another basic SAW device, a one-port SAW resonator is obtained by inserting one transducer between two reflector gratings as illustrated in Fig. 3.2. The resonance frequency, f_r, of the synchronous resonator is defined by the SAW velocity v_0 and the period p of the IDT, i.e., $f_r = v_0/2p$. Typical values for v_0 and p are in the range of 3000–4000 m/s and 1–20 μm, respectively. Adding one more transducer in between the two gratings, a two-port SAW resonator is obtained. This may also be considered as a bandpass filter with a very sharply peaked frequency response.
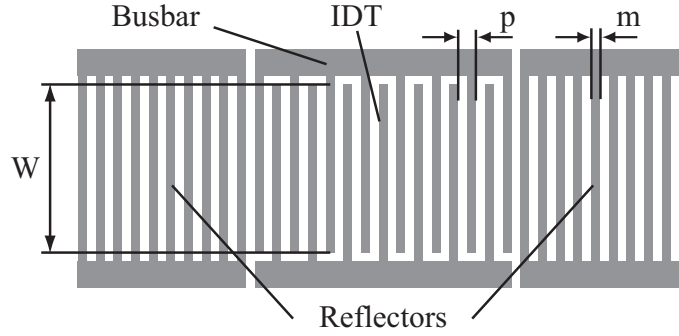
Figure 3.2: Illustration of a one port synchronous SAW resonator with pitch p, aperture W and width of the finger m.

More versatile devices are coupled resonator filters (CRF) [24, 25], which are also called double-mode SAW filters [26]. This structure is similar to two-port SAW resonators: a CRF contains three or more IDTs [27] surrounded by two reflectors on a piezoelectric substrate with strong electromechanical coupling. However, the operation principle is quite different since two resonance modes are excited: a symmetric and an antisymmetric mode. The filter features high rejection in the stopband, and a rather wide passband (typically 3–4 % of the center frequency) with low loss. In addition, the CRF is quite small and suitable for mass production. Due to these features, CRFs are widely used in the RF stage of a mobile-phone. A novel CRF design, a double-resonance filter, has been studied in [**III**]. The advantage of these filters is that they

offer a relatively narrow passband (1 to 2 % of the center frequency) with low insertion loss, steep skirts and improved suppression levels compared to conventional coupled resonator filters.

SAW resonators may also be used to build an impedance element filter (IEF). Impedance element SAW filters were introduced in 1993 [28], although the basic principle has been known and used in filters based on BAW resonators since the late 1920s [29]. In IEFs, one-port SAW resonators are connected electrically, with no acoustic interaction. Hence the resonators may be regarded as frequency-dependent impedances or impedance elements. These filters feature many advantages: low loss in the passband, high power durability, flat passband, small size, and steep passband skirts. However, the stopband rejection level is not as good as for the CRF, for instance.

Manufacturing SAW devices is based on the methods developed in the IC industry and hence the basic fabrication technique is optical lithography. The minimum linewidth obtainable is an important factor concerning the fabrication of SAW devices since it determines the maximum operation frequency. Very fine lines may be obtained by X-ray or electron-beam exposure [30, 31]. However, this is not yet commercially feasible. With standard optical lithography, high precision patterning of submicron scale can be achieved, with highly reproducible linewidths of less than 0.25 μm. To fabricate metal structures, an etching process or a lift-off technique [32] is used.

The upper frequency limit of the SAW technology can be pushed further by employing a longitudinal leaky SAW (LLSAW) [33, 34]. Due to the high phase velocity of the LLSAW in a periodic aluminum grating on the YZ-LiNbO$_3$ substrate ($v_0 \approx 6100$ m/s), the width of the finger electrodes in the IDT is larger than 0.25 μm even at frequencies above 5 GHz [35, 36]. This allows fabricating fundamental-mode SAW filters for frequencies as high as 5 GHz using standard optical lithography, employed in mass production of SAW devices. Furthermore, LLSAW manifests strong electromechanical coupling and low losses when propagating in a periodic aluminum grating on YZ-LiNbO$_3$. Hence it is a suitable propagation mode for low-loss wide-band filters [37]. In Publication [**I**], the acoustic wave fields in a LLSAW resonator have been studied using laser-interferometric measurements.

3.2   Imaging vibrations in SAW devices

The first papers about optical probing of SAW devices were published in 1967, soon after the invention of the IDT. These papers report the development of diffraction grating technique [38–42], knife-edge technique [43] and heterodyne interferometry [44] for measuring different parameters of SAWs, such as amplitude, velocity and attenuation.

In fact, all important SAW parameters can be measured using the above-mentioned techniques. Since the publication of the first papers, the diffraction grating technique was widely applied during the end of the 1960s and throughout the 1970s. Later on, the knife-edge technique and interferometry gained popularity during the 1980s and 1990s. The first review was written by Whitman and Korpel in 1969 [45], where they compared the different probing techniques. Since then, many excellent review papers and book chapters on optical probing of SAW have been published [46–52].

Many scanning laser interferometers for SAW imaging have been reported recently. One of these is a stabilized homodyne Michelson interferometer [53] that represents a typical performance of the modern setups. It is capable of recording both the amplitude and the phase of the vertical surface vibrations. The vertical resolution of the interferometer is about 0.3 pm, while the lateral resolution is diffraction-limited to approximately 0.5 μm. The frequency response is limited to 6 GHz by the bandwidth of the detector. The stabilization is achieved with a feedback system which locks the interferometer onto an interference fringe corresponding to an optical path difference giving the highest signal response. This is achieved by modulating the position of the reference mirror with 1 kHz frequency and using the interference signal at the second harmonic frequency of the mirror modulation (2 kHz) as an error signal to piezoelectrically control the position of the sample along the beam direction. Also a modified Mach-Zehnder laser interferometer [54], a heterodyne laser interferometer [55], and a Sagnac interferometer [56] have been reported. Another Sagnac interferometer with picosecond temporal resolution [57] has been used for imaging SAWs on phononic crystals [58]. A heterodyne Mach-Zehnder interferometer has been used for measurement of vibration fields in several SAW devices [59–61].

Two scanning laser inteferometers have also been constructed at TKK: a homodyne Michelson interferometer [6] and a heterodyne interferometer [62, 63]. Interferometric imaging at TKK was started in 1996 [64]. Since then numerous papers in reviewed journals and in the IEEE International Ultrasonics Symposia have been published by the research team at TKK [52,65,66]. More recently the laser interferometers have also been used for imaging surface vibrations in BAW resonators [11], in MEMS resonators [V,VI] and in phononic crystals [67].

The knife-edge technique is another optical method that has been widely used for imaging of SAWs. In that technique, a laser beam is focused on the surface of the sample with a lens, placed off-axis with respect to the laser beam. The reflection from the vibrating surface is collimated by the same lens and directed to a detector. A change in the angle of the reflected beam caused by the surface displacements of the SAWs is transformed into a parallel shift of the reflected laser beam. By blocking a part

of the beam with a sharp object, aka a knife edge, intensity modulation is generated, which can be detected at the photodetector. The advantage of this technique is that it does not require a reference beam and hence no stabilization scheme. It is also sensitive to the propagation direction of the surface wave. The knife-edge probe measures the component of the propagating SAW that is perpendicular to the edge.

The first knife-edge probe for the detection of SAWs was published in 1968 by Adler et al. [43]. Since then many different probes based on detecting the tilting of the surface have been published [68–78]. A commonly used optical setup with a balanced photodiode scheme is described by Engan [68,69]. In this setup, a separate knife edge is no longer needed and the number of components is reduced. In addition, using differential signal detection, the change in the light intensity due to varying reflectivity of the sample surface does not disturb the measurement. Moreover, both amplitude and phase of SAWs can be measured. Recently, a quadrant detector has been used to measure the vibrations in two orthogonal directions [76]. Also stroboscopic illumination by a picosecond-pulsed laser has been employed [70]. A fast scanning speed of 2500 points/s can be achieved by continuous sample movement [78] compared to the traditional point-by-point scanning (typically < 100 points/s). SAW devices can be further analyzed in the wavenumber domain by applying the fast Fourier transform to the measurement data containing amplitude and phase information [79].

Full-field imaging of thin film bulk acoustic wave resonators (FBAR) has been reported [80]. The measurement of the vertical displacement is based on dynamic holography with photorefractive interferometric detection. Using a charge coupled device (CCD) camera, both the acoustic amplitude and phase can be recorded over the surface of the sample with a data acquisition speed of 275 000 points/s. Laser speckle interferometry has also been employed to measure the vibrational distribution in SAW and BAW devices [81]. The vibrational distribution is obtained by applying image processing with two-dimensional correlation filtering of the speckle fields captured by a CCD camera. A CCD camera can also be used to directly visualize SAW on a piezo-electric semiconductor [82]. The method utilizes photoluminescence that is correlated to the SAW power.

Acoustic fields have also been mapped using optical microscopic reflectance and reflectance anisotropy [83]. The detection of SAWs is based on microscopic measurements of the reflectance changes and of the reflectance polarization anisotropy induced by the surface wave. The combination of these two techniques provides information about the longitudinal and transverse components of the SAW. Another optical method is based on the detection of the change in the polarization of the laser light transmitted through the SAW sample [84]. The polarization is affected by the strain of acoustic

waves through the photoelastic effect. Hence the setup is capable of detecting also the shear horizontal component of the LSAW. This technique was also applied to back-side observation of SAW under the electrodes [85] and to observation of waves propagating within the substrate [86].

SAWs may be visualized also with other than optical techniques, such as scanning acoustic force microscopy [87–95], scanning tunneling microscopy [96], scanning electron microscopy (SEM) [97–100] and X-ray topography [101–105]. In addition, direct visualization of SAWs using electromigration [106] and smoke particles [107] has been reported. Surface vibrations in FBARs have been measured using atomic force microscopy [108].

3.3 Acoustic loss mechanisms and transverse modes

Recently, acoustic loss mechanisms in synchronous one-port LSAW resonators have been under active study. It has been shown that the propagation loss of the LSAW on LiTaO$_3$ may be controlled by varying the electrode thickness and the crystal cut [109]. The influence of bulk-wave radiation on the IDT admittance on 42°YX-LiTaO$_3$ has been studied [110], and direct measurements of bulk acoustic wave (BAW) radiation in LSAW resonators on LiTaO$_3$ have been reported [111, 112].

One critical loss mechanism in LSAW resonators on rotated Y-cut LiTaO$_3$ is the leakage of LSAW into the busbar [113, 114]. The interferometric measurements of the vertical vibration amplitude showed asymmetric leakage of waves from the resonator [113]. Through numerical calculations, the asymmetry could be explained as asymmetry in the polarization of LSAWs propagating into different directions [114]. After that, the shear horizontal component of the LSAW was measured [84], confirming the computed LSAW polarization. Later, a structure to suppress the LSAW leakage was presented [115].

Different acoustic loss mechanisms in LSAW resonators on LiTaO$_3$ are thoroughly discussed in [116], including the LSAW leakage into busbars, coupling to BAWs and Rayleigh-wave radiation. However, the Rayleigh-wave radiation is only briefly discussed from a theoretical point of view. Rayleigh-wave radiation by a thin-film waveguide in the case of Love-wave propagation is treated in [117], but no experimental results are provided. In Publication [**II**], we have studied the Rayleigh-wave radiation both experimentally and theoretically.

Transverse waveguide modes in SAW devices are known to cause spurious resonances in the electrical response. First experimental observations were reported in 1975 using laser-probe [118] and electrical measurements [119]. It was shown that the

number of the transverse modes depends upon the width of the SAW resonator [119]. A simple model was proposed to facilitate a calculation of the transverse modes [120] by applying the optical waveguide model to SAW resonators.

The modes in SAW grating resonators and in grating waveguides have been studied using the paraxial wave equation [121, 122]. Particularly, the authors derived the transverse spatial profile of the modes that were experimentally verified [123] using a laser probe, but only the fundamental transverse mode was shown. Higher-order transverse modes in a two-port SAW resonator on ST quartz were observed using SEM [97]. To model the effect of transverse modes on the electrical response, several models [124–127] have been developed in addition to those mentioned above. Transverse modes have also been imaged using the Schlieren method [128]. The optical setup utilizes an internal reflection from the substrate to obtain acousto-optic diffraction of laser light. The particle displacement envelope is then observed with a CCD camera enabling large-area, real time visualization of vibration modes of SAW devices. Both symmetric and asymmetric transverse modes have been detected as well as their linear combinations.

Much work has been directed to suppress the transverse modes in SAW devices. Two methods were described and applied to a two-port SAW resonator on ST quartz already in 1976 [129]. The first was to reduce the acoustic aperture and the second was to use overlap weighting of the IDT. Later, more complicated structures were proposed [130, 131]. Self-suppression of the transverse modes can be achieved by using reflecting elements with positive and negative reflectivity [132]. These elements consist of electrically shorted and open strips. The suppression can also be achieved by using dummy electrodes between a busbar and the interdigital electrodes [133]. The dummy electrodes may be length- and width-weighted [134, 135].

The reason for the excitation of higher order transverse modes is the fact that the excitation profile is of different shape than the fundamental mode. Usually, the excitation profile is of rectangular shape while the waveguide modes are of sinusoidal shape. Many of the above mentioned techniques aim at changing the excitation profile to maximize the excitation of the fundamental mode. A different approach to suppress the transverse modes is to shape the transverse profile of the fundamental mode to match better to the rectangular excitation profile [136]. The transverse profile can be shaped by adding proper edge regions having lower wave velocity than the active transducer region. This was obtained by using a short-circuited grating with more electrodes per wavelength than the active center region. In Publication [**IV**], we have further developed the design of the edge region in R-SPUDT SAW filters. Laser interferometric measurements were carried out to validate the new design and the simulations.

3.4   Measurement results

3.4.1   LLSAW resonator

In Publications [**I**] and [**II**], we investigate a 1.5 GHz LLSAW resonator. An interesting feature of this resonator is the fact that the substrate supports two waveforms. Therefore, in addition to the LLSAW, also Rayleigh waves are excited within the same electrode structure, designed for LLSAW operation. Both the LLSAW and Rayleigh waves possess displacement components in the x and z directions, but for the LLSAW, the x component is dominating. The displacement component in the y direction is zero for both wave types. The displacement components of the Rayleigh wave decay exponentially into the bulk. However, the LLSAW is weakly coupled to the shear bulk wave, which has its displacement in the xz-plane. This bulk wave causes propagation losses for the LLSAW through radiating energy into the substrate.

The vertical vibration amplitude in the resonator was measured at 170 different frequencies around the resonance frequencies of the Rayleigh and LLSAW wave modes. The scan area of 110×484 μm^2 contains the whole resonator with 200×880 scan points and a scanning step of 0.55 μm. The input power fed into the resonator was +20 dBm for the LLSAW frequency range and -10 dBm for the Rayleigh frequency range. The measured vibration amplitude profiles at selected frequencies are presented in Fig. 3.3. In the light reflection image, metallized areas appear white whereas the free crystal surface of the YZ-LiNbO$_3$ substrate appears dark gray or black.

In the Rayleigh frequency range (left column of Fig. 3.3), the scanned frequency of 823 MHz is close to the resonance frequency of the Rayleigh waves. At 803 MHz and 813 MHz, a beating pattern in the profile along the longitudinal direction of the resonator is observed. The beating pattern, originating from interference between the excited acoustic field and the propagating eigenmode, typically occurs outside the grating stopband [18] for Rayleigh waves [137] and leaky SAWs. The number of antinodes increases as the frequency decreases. Above the resonance frequency at 830 MHz and 836 MHz, transversal modes are observed. The number of antinodes in the transverse direction of the resonator increases with frequency. At 862 MHz and 872 MHz, higher order transversal modes together with longitudinal beating patterns are present. In all the scanned images in the Rayleigh frequency range, the waves propagate through the reflector gratings. This is due to the small reflection coefficient per electrode for Rayleigh waves. The reflectors are relatively short since the resonator is designed for LLSAW, and therefore, they fail to confine the acoustic energy into the resonator at the Rayleigh frequency range.

In the LLSAW frequency range (right column of Fig. 3.3), the amplitude profile at
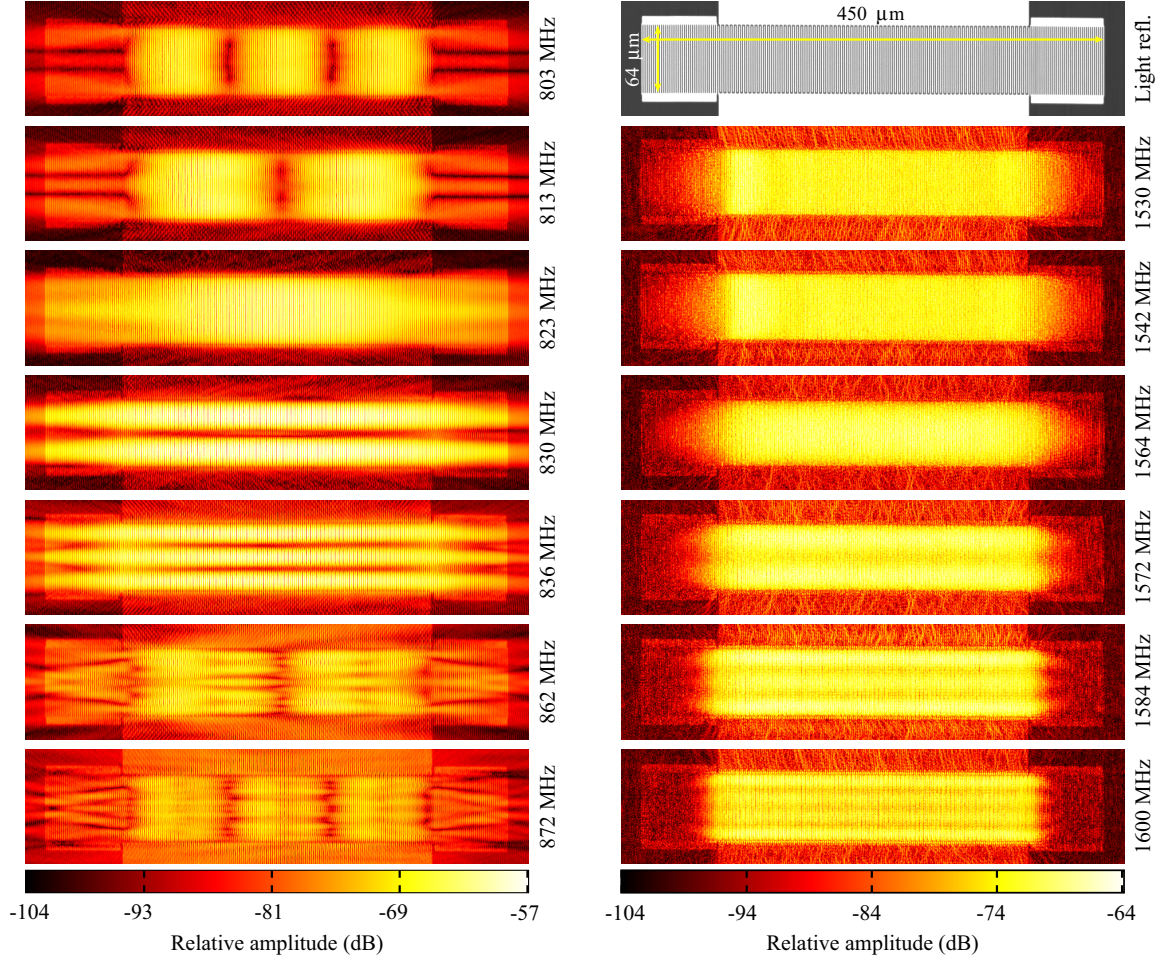
Figure 3.3: Measured vertical vibration fields at selected frequencies for the Rayleigh waves (left) and for the LLSAW (right). The interferometer signal measured by the spectrum analyzer (in dBm) represents the power density of SAW, i.e., when the relative amplitude increases by 6 dB, the acoustic displacement is doubled. The upper right corner shows a light-reflection image of the resonator.

1542 MHz is close to the electrical resonance frequency. At the frequencies 1450–1540 MHz, i.e., below the lower edge of the grating stopband, longitudinal beating patterns are not observed. This may be due to the high reflection coefficient per electrode for LLSAW rendering the interactions of the LLSAWs along the resonator more localized. The beating pattern typically occurs outside the stopband for Rayleigh waves [137] and leaky SAWs, and in this sense the behavior of LLSAW appears different. Above the

LLSAW resonance frequency, transversal modes are observed at 1572 MHz, 1584 MHz and 1600 MHz although there are no peaks visible in the electrical response at these frequencies [**I**]. Strong attenuation of the LLSAW in the reflectors at both ends of the IDT is observed due to the high value of the reflection coefficient per electrode. The penetration depth of the LLSAW into the reflector decreases with increasing frequency in Fig. 3.3, as the frequency approaches the center frequency of the grating stopband where the reflector operates most efficiently.

The complete chip containing the LLSAW resonator was also scanned at numerous frequencies around the Rayleigh and LLSAW frequency ranges. The scan area of 740×1240 μm^2 contains 560×940 data points with a scan step of 1.32 μm. Figure 3.4 shows the scans at selected frequencies. The scans reveal the presence of distinct acoustic beams radiated from the resonator and propagating with low attenuation. In Publication [**II**], we propose that these beams are Rayleigh waves emitted from the resonator. This side radiation of Rayleigh waves is generated by the transverse electric field in the end gap between the busbar and the electrode due to oscillating charges accumulated on the electrode fingertips of the IDT. This periodic line of point sources oscillating in phase generates the beams both in the direction perpendicular to the IDT and the higher order beams in the oblique directions.
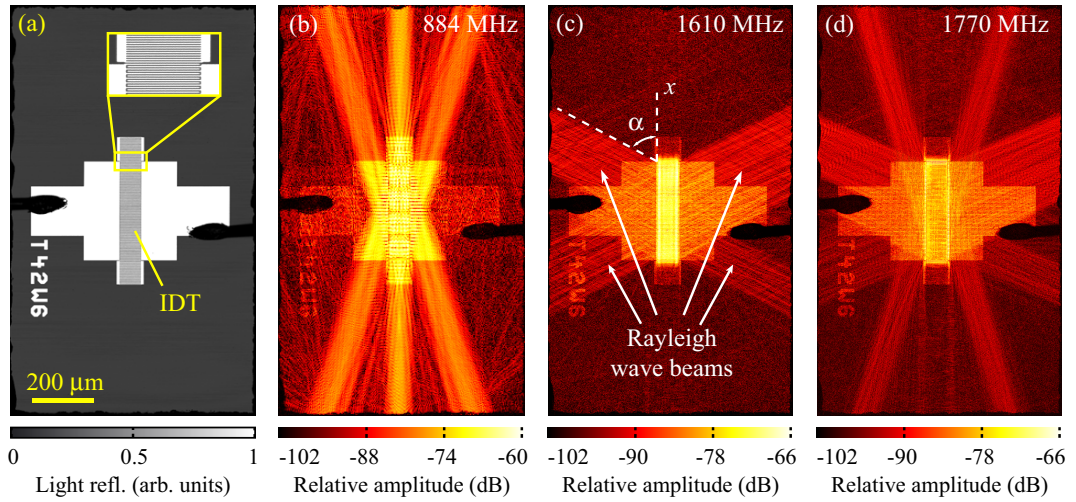

Figure 3.4: Laser-interferometric scans of the LLSAW resonator: (a) light-reflection image and (b)-(d) vertical amplitude fields revealing Rayleigh wave beams emitted from the resonator. The sensitivity of the interferometer is different on crystal, metal and grating surfaces leading to a discontinuity of the amplitude at the boundary between these areas.

Figure 3.4(b) depicts a scan in the Rayleigh frequency range of the LLSAW res-
onator. Four oblique beams of Rayleigh waves are emitted from the side of the resonator
at an angle of $\alpha \approx 20°$ with respect to the longitudinal direction (the x direction). The
additional beams at $\alpha = 0°$ are due to the waves propagating through the reflector grat-
ings. In Fig. 3.4(c), the four Rayleigh wave beams are emitted to an angle of $\alpha \approx 61°$.
At this frequency, the beams in the perpendicular direction ($\alpha = 90°$) are also distin-
guishable. At higher frequencies, four more oblique beams appear. These beams are
the second order Rayleigh wave beams. For example, at 1770 MHz in Fig. 3.4(d), the
beams are radiated to the angles of $18°$ and $67°$. The additional beams at the angle
of approximately $0°$ with respect to the longitudinal direction are due to a part of the
second order Rayleigh wave beams being waveguided by the reflector busbars.

In Fig. 3.5, the radiation angles extracted from the interferometric measurements
are compared to the theoretical radiation angles. The theoretical values are approx-
imated using the synchronism condition between the grating wavenumber and the x
component of the Rayleigh wave's wavenumber [II]. The experimental radiation angle
at each specific frequency was obtained by averaging the radiation angles determined
from all the four beams radiated symmetrically. The numerical calculations of the
energy flow direction (solid line in Fig. 3.5) yield angles that agree well with the ex-
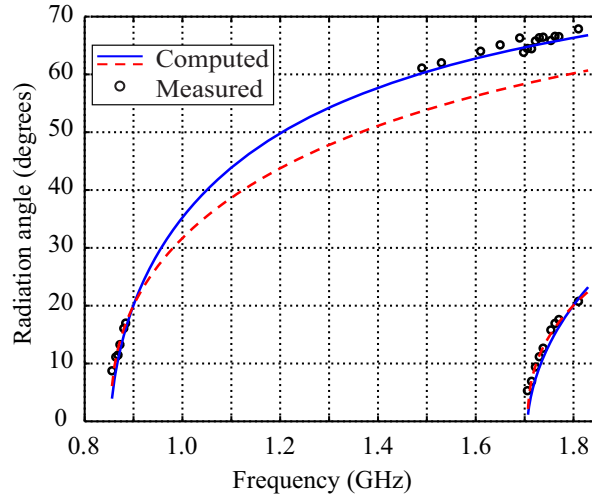perimental observations. The dashed line shows the computed direction of the wave

Figure 3.5: Measured and calculated angles of radiation versus frequency
for Rayleigh SAW emanating from the LLSAW resonator. The solid line is
the computed direction of the energy flow (group velocity) and the dashed
line is the computed direction of the wave vector (phase velocity).

vector that differs from the energy flow direction due to the anisotropy of the YZ-LiNbO$_3$ substrate.

Usually the leakage of acoustic waves deteriorates the filter performance through increasing the losses by carrying energy away from the device and also through acoustic crosstalk between the resonators in impedance element filters. However, in the case of the Rayleigh-wave radiation studied in [II], the effect probably is too small to cause significant losses that would deteriorate the electrical response of the resonator or that of the filter. Nevertheless, the interferometric measurements presented here reveal invaluable information of the Rayleigh wave radiation and verify the excitation mechanism of that through comparison between theory and experiments.

3.4.2   Double-resonance SAW filter

Two samples of a double-resonance structure were measured: a resonator and a filter. The structure consists of two long IDTs (input and output IDTs) separated by short transducer sections constituting a distributed gap [III], see Fig. 3.6. A strong localized resonance, called a hiccup resonance, is formed in the gap region, in addition to the resonance arising in the long structures - hence the name double-resonance filter. The filters satisfy the specifications used in the Global Positioning System (GPS).
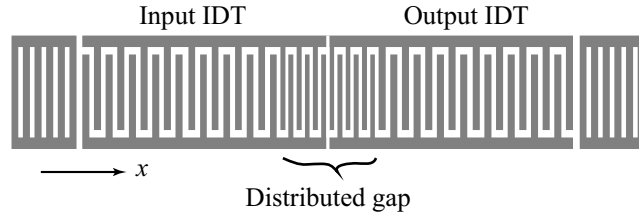
Figure 3.6: Topology of the double resonance filter. The distributed gap consisting of short transducer sections is placed between the long transducers, surrounded by reflector gratings.

Similar measurements were carried out for both samples. First, laser-interferometric measurements with a large scan step (1.7 μm) were conducted over a frequency range 1480 MHz – 1690 MHz with a frequency step of 2 MHz in order to get an overview of the device operation. Based on these measurements, a set of the most interesting frequencies were selected for more detailed scans: 27 frequencies for the filter and 30 frequencies for the resonator. The detailed scan area of 330 μm × 128 μm contains 1000 × 130 data points with a scans steps of 0.33 μm and 0.99 μm, respectively.

An areal scan of the double-resonance filter measured with a detailed scan step at 1542 MHz is shown in Fig. 3.7. In the light-reflection image (Fig. 3.7(a)), the finger structure of the IDTs and the reflector gratings are still resolved although the periodicity of the structure is close to the spot size of the laser beam. In the amplitude image (Fig. 3.7(b)), strong vibrations are observed in the left IDT, which is the input transducer of the filter. The amplitudes in the input IDT are larger than the amplitudes in the region of the distributed gap because the selected frequency is close to the synchronous resonance. Furthermore, the vibration amplitude in the input IDT is 16 dB larger than that in the output IDT.
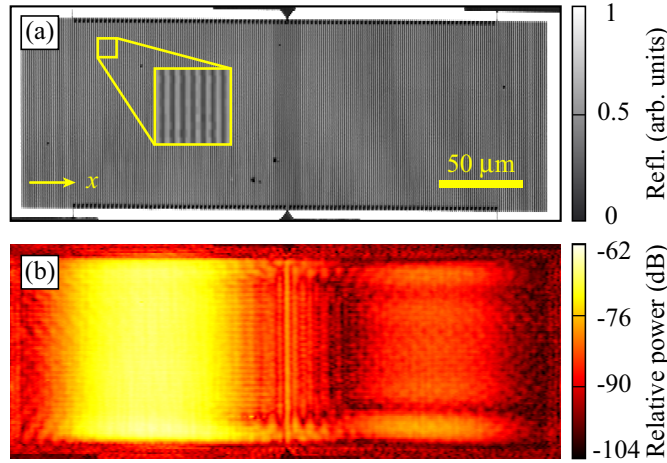
Figure 3.7: Laser-interferometric scan of a double-resonance filter at the frequency of 1542 MHz: (a) light-reflection image and (b) relative amplitude of the vertical vibration component.

The interferometer data are filtered in the Fourier domain to remove the standing wave pattern and the contributions caused by the high and low optical reflectivity of the finger structure. In other words, the measured amplitude distribution, converted to linear scale, is Fourier transformed, and high spatial frequencies corresponding to the periodicity of the finger structure are suppressed. Finally, an inverse Fourier transformation is applied and the filtered data are converted back to dB-scale. Hence, the envelope of the acoustic wave fields is obtained.

To allow comparison of the measured and simulated vibration amplitudes, line profiles were plotted. The simulations were carried out using the coupling-of-modes (COM) model [19, 138]. The experimental line profiles were extracted from the center of the areal scans by averaging 70 longitudinal lines, i.e., lines in the x direction. The simulated frequencies were chosen such that the best match between the simulations and
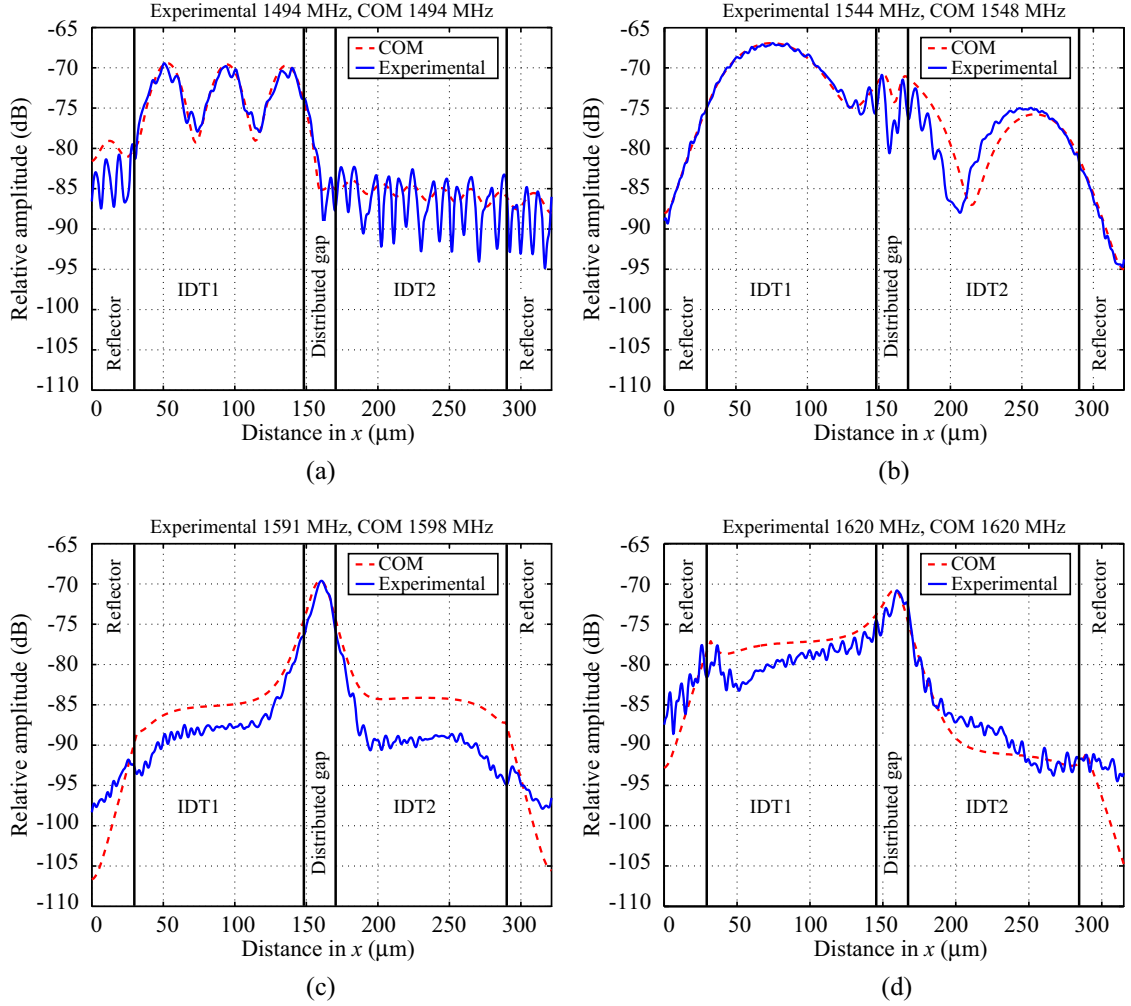
Figure 3.8: Simulated and measured line profiles of the SAW amplitude distribution in the double-resonance filter. The input power was +10 dBm for (c), +20 dBm for the others.

measurements was found. The simulated curves were also shifted in vertical direction so that the maximum of the simulated line profile coincides with that of the experimental curve. The line profiles of the double-resonance filter are shown in Fig. 3.8. Below the grating stopband, mode patterns with multiple antinodes arise. The profile in Fig. 3.8(a) shows such a pattern. The synchronous resonance, with acoustic amplitude distributed in the long transducers, is shown in Fig. 3.8(b), and the hiccup resonance having the energy concentrated in the distributed gap is depicted in Fig. 3.8(c). Figure 3.8(d) shows the amplitude distribution above the filter passband.

The filter operation is clearly identified in the profiles of Fig. 3.8. In the filter stopband, amplitudes in the input (IDT 1) are higher than the amplitudes in the output (IDT 2), see Figs. 3.8(a),(b) and (d). Around the frequencies of the synchronous resonance, Fig. 3.8(b), the high acoustical reflectivity of the long transducers prevents the propagation of the SAW inside the structure from the input port to the output port. Therefore, the strong acoustic field arising in the input IDT is not effectively transferred to the output IDT, and no electrical response is created [III]. Only at the frequency of the hiccup resonance, Fig. 3.8(c), the strong resonance arising in the gap region serves to transfer energy from the input IDT to the output IDT. Consequently, an electrical response with a narrow bandpass and high suppression levels in the filter stopband can be obtained.

The interferometric measurements presented here serve to validate the operation principle of the device and confirm the results obtained by simulations. The measured acoustic profiles are mostly in good agreement with the COM simulations. Differences in the details of the amplitude levels can be observed, but the shapes of the measured profiles fit well to the simulated ones. The differences may be caused by parasitic effects and matching conditions, since the input resistance is not taken into account in the simulations of the acoustic amplitudes. The measurements also confirm that a considerable part of the acoustic energy is concentrated in the gap area at the hiccup resonance frequency. This may limit the power handling capability of the filters.

3.4.3   R-SPUDT filter with transverse mode suppression

Two versions of the same SAW R-SPUDT filter design for mobile phone base station applications were studied in [IV]: a standard device without transverse mode suppression and a piston-mode device with transverse mode suppression. The suppression of transverse modes is achieved by implementing an edge region in the R-SPUDT filter, in which case only one transverse mode is efficiently excited as discussed on p. 16. The edge regions were implemented by using a higher mark-to-pitch ratio as illustrated in Fig. 3.9. The interferometric measurements were carried out for 49 frequencies in the frequency range 198.83 MHz – 199.97 MHz with a frequency step of 0.02 MHz.

The dimensions of the filters are approximately 10 mm × 1.2 mm, while the finger period in the x direction is relatively small, approximately 4–8 μm. This results in complementary requirements for the scan parameters: the scan step should be small enough to resolve all the details (fingers), while on the other hand, the large size of the device would require a large scan step to keep the scan time (and data amount) reasonable. In practice, this means that it is not feasible to measure the whole device with high resolution. Therefore, seven smaller scan areas were chosen, containing

Figure 3.9: Schematic view showing a part of the piston mode device. The width of the fingers (gray in the illustration) is wider in the edge region than in the center region.

300×120 scan points with scan steps of 0.99 μm and 9.90 μm in the x and y directions, respectively.

Figure 3.10 shows the measured and simulated acoustic amplitude fields for one of the longitudinal main modes in the piston-mode device. The amplitude field appears flat in all scan areas and matches quite well the simulated amplitude field. The frequencies corresponding to the main mode were selected by locating peaks in the electrical responses. There is a frequency offset of 0.1 MHz between the measured and simulated frequency responses [**IV**].
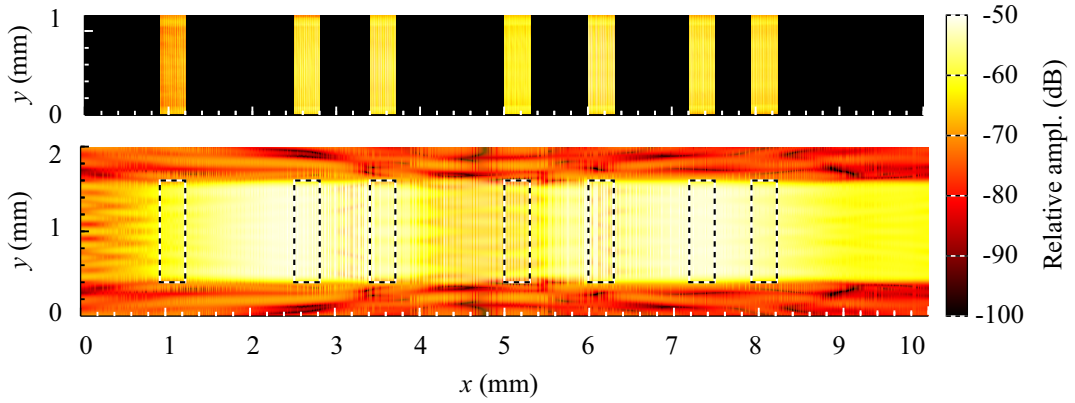
Figure 3.10: Acoustic wave field of a longitudinal main mode in the piston-mode device: measurement at 199.01 MHz (top) and simulation at 198.91 MHz (bottom). The dashed rectangles in the simulated amplitude image indicate the areas corresponding to the scanned areas.

To illustrate the effect of the edge design on the transverse amplitude profiles, Fig. 3.11 shows the measured and simulated transversal amplitude profiles for one of the longitudinal main modes in the standard and piston-mode devices. The measured amplitude profiles were obtained by averaging all the scan lines between $x = 2.5$ mm and $x = 2.8$ mm. In addition, the simulated curve was shifted such that the maximum values of the measured and simulated curves coincide. The discontinuities in the measured profiles are due to the difference in the optical reflectivity of the transducer and busbar surfaces.
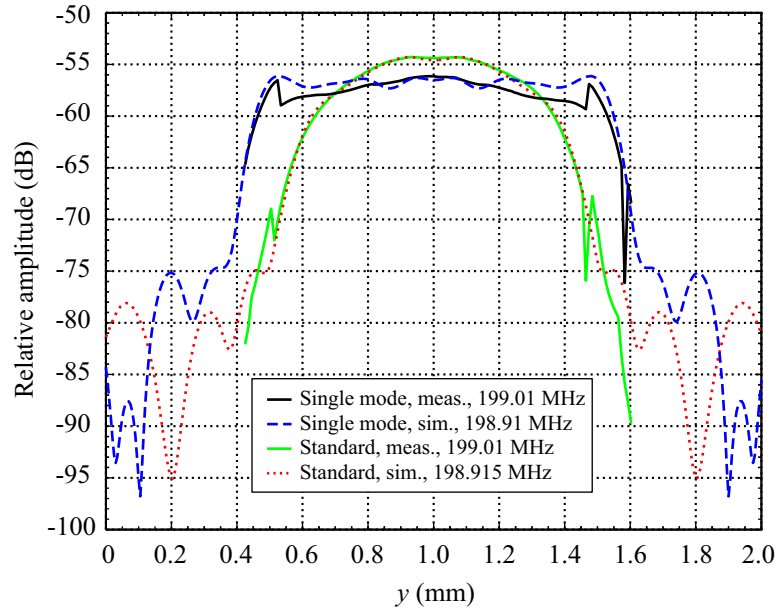
Figure 3.11: Measured and simulated transverse profiles of the acoustic amplitude for the standard and piston-mode devices at $x = 2.65$ mm. The discontinuities in the measured curves are due to the difference in optical reflectivity between the edge and center regions.

The correspondence between the measurement and simulation is excellent for the standard device where the mode shape is smooth and round in the y direction. For the piston-mode device, the measured profile is slightly less rectangular than that predicted by the model. This indicates that the velocity in the edge region is probably underestimated. This would also explain why remaining transverse mode effects are seen on the electrical filter response [**IV**]. The experimental results of the acoustical amplitudes validate both the simulations and the successful application of the new design for the SAW filter with transverse mode suppression.

4   Microelectromechanical systems

Microelectromechanical systems (MEMS) are, in general, micrometer-scale devices where mechanical movements or vibrations are driven by electrical signals. The first MEMS devices appeared in the 1960s after the basic processing technologies, such as silicon anisotropic etching in alkaline solutions [139], were developed. For example, a piezoresistive silicon diaphragm for pressure sensing was developed in the 1960s [140] and has been widely used since. The first demonstration of a micromachined silicon accelerometer [141] was reported in 1979. In the 1990s, they were commercialized for automobile air bag systems by Analog Devices [142] and nowadays they are produced in large quantities.

Another successful example is a concept in projection display technology referred to as Digital Light Processing^{TM} (DLP) developed by Texas Instruments. DLP is based on a matrix of micromirrors on a semiconductor chip, known as the Digital Micromirror Device^{TM} [143]. This device was invented in the early 1980s [144] while the first product family of DLP-based projection systems was introduced in 1996. Other commercial MEMS applications may be found in many fields, such as in photonics, life sciences and RF systems [145]. In industrial applications, gyroscopes, micropumps, fluid nozzles, and thermal inkjet heads serve as examples as well as MEMS switches, inductors, capacitors, filters, phase shifters, transmission lines and antennae that have been developed for RF systems over the years [146–148].

The most common material for MEMS is single crystal silicon due to its excellent electrical and mechanical properties [149]. Silicon can also be economically manufactured in single crystal substrates, and hence these substrates are relatively low cost (approximately 10 $ for a wafer with a diameter of 100 mm [145]). In addition, the opportunity to use the huge industrial infrastructure of the electronic IC industry in manufacturing gives an economical advantage compared to other materials. Other substrate materials for MEMS are glass, fused quartz, silicon carbide, diamond, gallium arsenide, and some polymers, such as polypropylene.

To fabricate MEMS, there are several process tools that can be applied [145]. Uniform layers of semiconductors, metals, insulators, and polymers can be deposited using techniques such as epitaxy, sputtering, evaporation, and chemical vapor deposition. Optical lithography combined with etching is used for removing material at selected places to achieve the desired microstructure. Especially, dry processes such as reactive ion etching and chemical vapor deposition play important roles in MEMS fabrication [150].

4.1   MEMS resonators

MEMS devices that make use of mechanical resonances in the structure have been actively developed since the 1960s. For example, the resonant-gate transistor [151,152] and an oscillator based on the "resonistor" [153] utilized the resonance of a micromechanical cantilever beam. Recently, MEMS resonators have been developed for diverse applications, such as for oscillators [154], filters [154–156], sensors [157] and gyroscopes [158].

One of the earliest surface-micromachined resonator designs, which has been commonly used in various MEMS devices, is the laterally driven polysilicon resonator [159]. The structure consists of an interdigitated-finger comb-drive and folded springs supporting a plate that oscillates in the plane of the wafer surface. Another common type of MEMS resonator is a silicon cantilever that is used in AFM, for instance. In the dynamic mode of AFM, the cantilever is oscillating at a frequency of a few kHz.

Another MEMS resonator, a bulk-acoustic-mode beam resonator [160] is depicted in Fig. 4.1. The resonator consists of a silicon beam supported in the middle and vibrating in the x direction with amplitude u_x, as illustrated in the figure. This is the so-called in-plane vibration mode. The resonance frequency of the resonator is 12 MHz with a quality factor (Q) of 180 000. Also out-of-plane modes (e.g. flexural modes) with vibrations mainly in the z direction can be excited in this kind of structures.

Many variations of the beam resonator exist. For example, a tunable single-crystal silicon beam resonator, reported in [161], is designed such that its resonance frequency (≈ 1 MHz) can be tuned in a range of 60 kHz with a DC voltage. Beam resonators with both ends moving freely or with both ends clamped have also been demonstrated [162]. With a similar structure but operated in the second harmonic flexural vibration mode [163], Q on the order of 12000 at 101 MHz has been achieved.
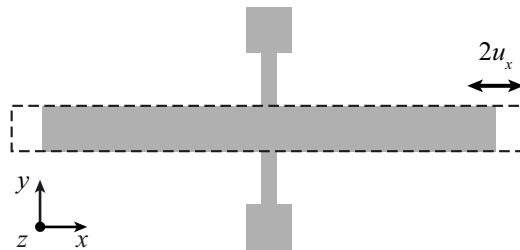
Figure 4.1: MEMS beam resonator.

4.1.1 Square-plate resonator

The square-plate MEMS resonators, studied in this work, have been designed and fabricated at VTT Technical Research Center of Finland. The resonators possess a resonance frequency of 13.1 MHz, a high quality factor of 130 000 (in vacuum and with a bias voltage of 100 V) and a high power handling capacity of 0.12 mW [164]. An oscillator based on such a resonator is an attractive alternative for the quartz reference oscillator in portable applications due to its low phase-noise, compact size, low power consumption and integrability with IC electronics.

The resonator, illustrated in Fig. 4.2, consists of a 10 μm thick square plate released from the silicon substrate and supported at the corners with springs. The size of the resonator plate is 320μm × 320μm. The device has been fabricated using deep reactive ion etching on a silicon-on-insulator wafer. For the sacrificial oxide release etch, a 39×39 grid of circular holes (diameter 2 μm) was fabricated in the resonator plate, see Fig. 4.2(b).
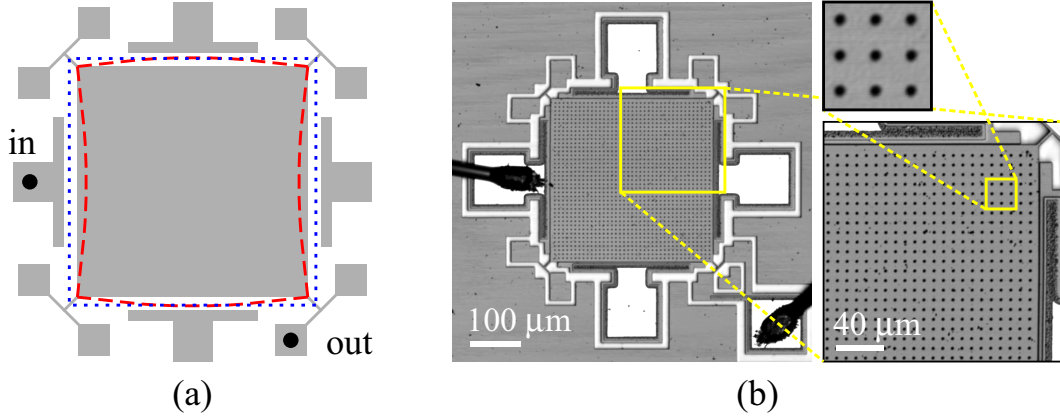
Figure 4.2: (a) Schematic drawing of the micromechanical resonator. The square-extensional mode and the Lamé mode are illustrated with dotted and dashed lines, respectively. (b) light-reflection images of the resonator showing the release-etch holes.

The resonator is excited capacitively using electrodes placed on all four sides of the square plate. Hence, the excitation is mainly in-plane. However, in this work only one of the electrodes was connected to enable excitation of a wider variety of vibration modes [**VI**]. The main vibration mode of the resonator, the square-extensional (SE) mode, is described as a two-dimensional expansion preserving the plate's original square shape. The dotted line in Fig. 4.2(a) illustrates the expanded shape of the square plate

in the SE mode. With the one-electrode drive, the resonator also exhibits the Lamé mode. In the Lamé mode, illustrated with the dashed line in Fig. 4.2(a), the edges of the square plate bend in antiphase preserving the volume of the plate. In both cases, the motion is mainly in plane but vibrations perpendicular to the surface are also excited due to the non-zero Poisson ratio of the silicon crystal.

To enable laser-interferometric measurements in vacuum, a custom-made sample enclosure was designed and built during this work [165]. The resonator was enclosed in a small metal case connected to a vacuum pump. The case has a quartz window, through which the measurement beam of the interferometer is focused by a microscope objective onto the surface of the resonator.

Figure 4.3 shows the electrical response of the resonator (S_{21} element of the scattering matrix [166]) measured in ambient air pressure and in vacuum (pressure below 1 mbar). The resonance frequencies of the Lamé and SE modes are 12.13 MHz and 13.10 MHz, respectively. Typically, electrical Q values can be estimated from the S_{21} response by determining the 3 dB width of the resonance peak. However, since the response of the device is weak in this case, the electrical Q values were determined by fitting the response of an electrical equivalent circuit model to the measured electrical response. The electrical equivalent circuit consists of a series resonant circuit that is connected in parallel to a stray capacitance [164]. The electrical Q values were calculated from the parameters of the fitted equivalent circuit and they were found to be 37 000 and 87 000 in vacuum for the Lamé and SE modes, respectively.

Mechanical vibrations in the resonator may be approximated with a simple theoretical model [164]. The equation of motion for a lumped mass-spring system is

$$M\frac{\partial^2 x}{\partial t^2} + \gamma\frac{\partial x}{\partial t} + Kx = f(t), \tag{4.1}$$

where K is the effective spring constant, M is the effective mass, γ is the damping coefficient, and $f(t)$ is the driving force. The vibration amplitude, $x(t)$, and the driving force, $f(t)$, are assumed to vary sinusoidally in time t, that is, $x(t) = Xe^{i\omega t}$ and $f(t) = Fe^{i\omega t}$, where X is the amplitude of the vibration, F is the amplitude of the driving force and ω is the angular frequency. Substituting $x(t)$ and $f(t)$ into Eq. (4.1), the vibration amplitude is

$$|X| = \frac{F/K}{\sqrt{\left(1 - \frac{\omega^2}{\omega_0^2}\right)^2 + \left(\frac{\omega}{Q\omega_0}\right)^2}}, \tag{4.2}$$

where $\omega_0 = \sqrt{K/M}$ is the angular resonance frequency and $Q = \omega_0 M/\gamma$ is the mechanical quality factor. This simple model is later used to extract Q from the laser-probe measurements.
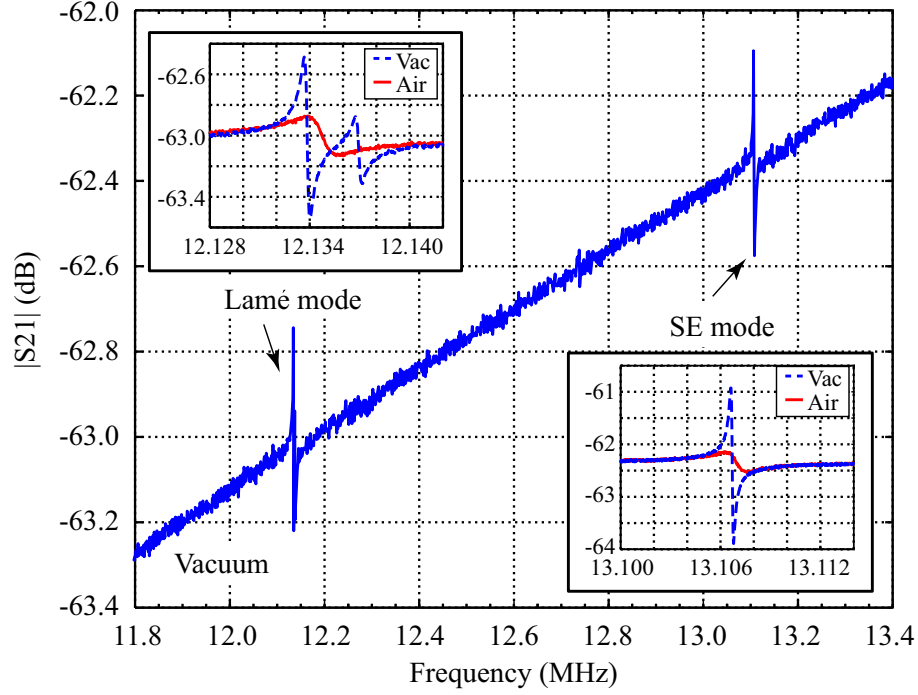
Figure 4.3: Electrical response of the resonator attached to a circuit board. The response, showing both the Lamé and SE modes, was measured with an input power of 0 dBm and a bias voltage of 60 V.

4.2 Imaging vibrations in MEMS devices

Many authors have conducted measurements of the mechanical frequency response at a single spatial point, for example, to obtain the resonance frequency and quality factor of a MEMS resonator [167]. In this section, an overview of measurement systems capable of mapping vibration fields and mode shapes in two dimensions is presented. A good review on methods used to characterize static displacements, motions, vibrations and internal strain in micromechanical devices can be found in [168].

As discussed in Section 3.2, vibration imaging systems for SAW and BAW devices have existed for a long time. As MEMS has recently gained interest, imaging vibrations in MEMS devices has also become relevant. With SAW devices, sensitive broadband measurement systems are needed due to the small vibration amplitudes and high operation frequencies. With MEMS, the low frequencies and large vibration amplitudes have made it possible to build relatively low-cost measurement systems, that are commercially available. Additionally, the use of characterization equipment, such as SEM and AFM, may prove to be useful for the detection of vibrations in MEMS devices.

Many MEMS devices utilize in-plane vibrations in their operation. Hence, the measurement of in-plane vibrations is important in MEMS research. Light microscopy can be used to measure both in-plane and out-of-plane vibrations. The basic idea is to acquire still images of a target structure using a light microscope, CCD camera and stroboscopic illumination [169]. In-plane motion down to nanometer-scale amplitude can be determined directly from these images using computer vision algorithms. Furthermore, a CCD camera enables the measurement of the whole image simultaneously without point-by-point scanning. In-plane vibrations in MEMS devices have also been measured using correlation of synchronous images [170, 171] and by employing continuous illumination and a high-speed camera with a frame rate up to 32000 frames per second [172]. In addition, a video microscope with continuous illumination has been used to measure the in-plane vibration of a target, such as the edge of a shuttle mass of a MEMS resonator [173]. In this system, the vibration amplitude is obtained by comparing a single time-integrated blur image of the device in motion to an image of the device at rest.

Out-of-plane vibrations can be measured with subnanometer resolution using interference microscopy [174, 175]. Here, the light from the stroboscopic source is divided onto a target and a reference mirror as in Michelson interferometer. The frozen interference fringes are captured by a CCD camera and are used to generate time-resolved surface-height maps. Stroboscopic phase-shift interferometry [176, 177], microscopic interferometry [178] and electronic speckle pattern interferometry [179–181] have been used for the same purpose. Combining the above mentioned techniques, a full 3-dimensional (3D) motion characterization of MEMS devices can be carried out [174, 182–184].

Commercial laser Doppler vibrometers [185] have been quite popular for measuring the frequency response of vibrating MEMS devices at a single point. Typically, their upper frequency limit has been from 100 kHz to a couple of MHz, but vibrometers with frequency range up to 30 MHz have become available recently, and performance even up to 500 MHz has been reported [186]. Combining this kind of equipment with 2D translation stages, out-of-plane mode shapes and resonance frequencies of a micromachined silicon cantilever and a bridge have been measured [187]. A similar system was built for directly measuring out-of-plane displacement maps in MEMS ultrasonic transducers [188]. Also mode shapes of a piezo-actuated silicon cantilever have been measured using a commercial scanning laser Doppler vibrometer [189]. Combining a scanning laser Doppler vibrometer and a confocal microscope, high lateral and depth resolution (spot size of 430 nm) can be achieved with picometer amplitude resolution [190]. In-plane vibrations can be measured using a differential laser Doppler system [191].

Optical profilers based on white light interferometry have been used for a long time to measure surface features and profiles of static samples. Replacing the continuous white light source with a stroboscopic light source, a commercial optical profiler can be modified to enable measurements of moving structures [192]. With such an instrument, the out-of-plane vibration amplitude and phase of a MEMS device can be measured [193,194]. The typical frequency range up to a few MHz and resolution in the nanometer range can be slightly improved by utilizing a signal deconvolution algorithm for correction of the strobed light response [195].

The minimum detectable out-of-plane vibration amplitude of many of the above discussed techniques is limited to the nanometer range. Reasons for this may be the noise and the dynamic range of the CCD camera. Using photodetectors, the sensitivity can be improved to picometer range. The disadvantage of this approach is that the measurement of a vibration field must be carried out point by point using mechanical translation stages or optical scanning. This decreases the measurement speed compared to systems employing a CCD camera. Recently, scanning interferometers have been utilized to characterize out-of-plane vibrations in MEMS devices. In [196], the authors report measurements of a MEMS mirror carried out using a stabilized Michelson interferometer with a frequency range up to GHz. Micromachined ultrasonic transducers have been measured using heterodyne interferometers [197, 198] and a homodyne Mach-Zehnder interferometer [199].

Feedback interferometry has been employed to measure (at a single spatial point) the resonance frequency, the quality factor and the actuation efficiency of MEMS resonators [200, 201]. The method is based on detecting the amplitude and frequency modulations of output signal arising from the laser oscillation when a small part of the light is reflected back into the laser from the vibrating sample. The monitor photodiode of the laser provides the output signal of the interferometer. In the setup, the device under test was positioned at an angle of 20° with respect to the laser beam and the vibrations were measured along the laser beam axis. By using multiple beams, or by making different measurements at different beam orientations, it is possible to reconstruct the vibration amplitude in three orthogonal directions.

As discussed above, optical techniques provide several possibilities to study the mechanical behavior of MEMS devices with a sensitivity down to the picometer range. In some cases, however, a better lateral resolution is needed than that provided by the optical techniques, i.e., much less than 1 μm. Therefore, researchers have applied other techniques, such as SEM and AFM, to measure vibrations in MEMS. For example, SEM has been used to determine the in-plane vibrations and the dynamics of micromachined lateral suspensions [202]: spectral analysis of the frequency components and

the damping using a ring-down measurement. Also the amplitude distribution of the different modes can be obtained. The resolution of this technique is limited by the diameter of the electron beam that is on the order of nm. The frequency range is limited to few hundred Hertz due to the increased shot noise of electron sources compared to photon sources. The frequency range can be increased to few MHz using stroboscopic illumination achieved by time-gated sampling of the secondary electron signal [203].

Dynamic characterization of oscillators based on nanoelectromechanical systems (NEMS) have been studied using AFM [204]. The obtained resonance frequency and the vibration amplitude at the resonance are compared to corresponding values obtained by an optical probe, showing that the resonance frequency of a NEMS cantilever could be obtained correctly. However, the quality factor determined with the AFM is about an order of magnitude lower than that measured with the optical probe due to the mechanical damping caused by the AFM probe. The authors also study theoretically the interaction between a coupled NEMS resonant cantilever and the AFM cantilever. In dynamic force microscopy [205], the second eigenmode of the AFM cantilever is employed for the detection of vibrations. In the paper, the method is demonstrated with a thin film bulk acoustic wave resonator operating at 1.6 GHz. The spatial resolution is in the nanometer and the sensitivity in the subnanometer range.

4.3 Detection of in-plane vibrations

A method was developed during this work to measure in-plane vibrations in addition to the out-of-plane component using the same setup. The method is based on observing the intensity modulation caused by an in-plane surface vibration at the position of a reflectivity gradient on the sample surface. In this work, the etch-hole structure of the MEMS resonator was utilized for this purpose as depicted in Fig. 4.4 for one lateral dimension. In the figure, a laser beam focused on the sample surface is partially reflected back from the edge of an etch hole. Also other contrast features on the sample surface (e.g., metal dots) could be utilized as well as edges of the resonator plate itself [206].

Figure 4.5 shows the dependence of the back-reflected optical power on the relative position of the laser beam to the etch hole. The crosses in the figure indicate measured values, whereas the solid line represents a fit of a theoretical curve to the measurement data. The theoretical curve is obtained by considering the reflection of a Gaussian laser beam from a sharp edge in one dimension. The total power in the reflected portion of
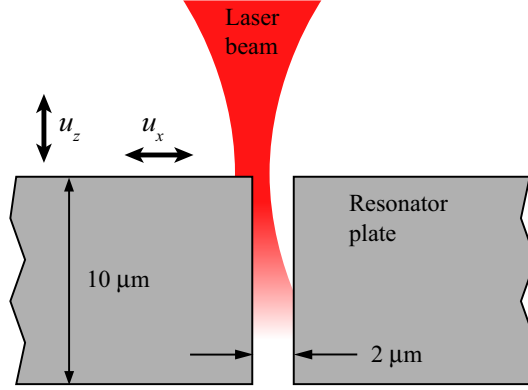
Figure 4.4: Cross section of an etch hole in a MEMS resonator.
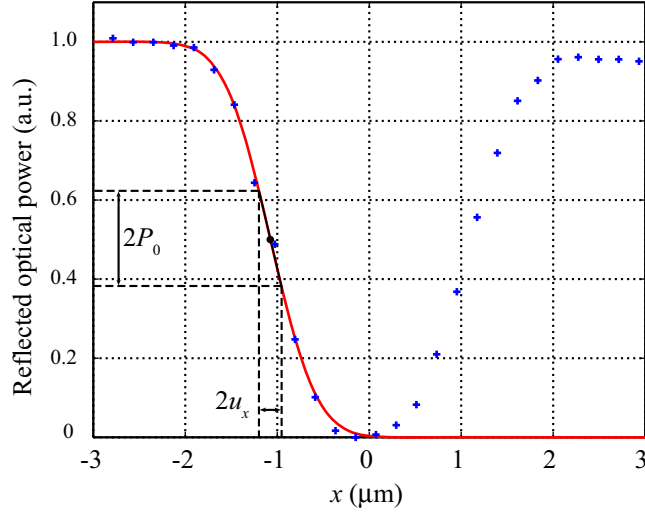
Figure 4.5: Intensity of the laser beam reflected from the sample when the beam is scanned across an etch-hole, measurement $(+)$ and fit $(—)$.

the beam is proportional to the complementary error function [10],

$$P(x) = \frac{1}{2}\left(1 - \mathrm{erf}\left(\sqrt{2}\,\frac{x - x_0}{w_0}\right)\right), \tag{4.3}$$

where x is the position of the center of the incident beam, x_0 is the position of the edge and w_0 is the waist size of the Gaussian beam. This one-dimensional function matches well the measured values, even though in our case the beam width $(2w_0)$ and the hole diameter are of the same order of magnitude, 1.6 μm and 2 μm, respectively.

If the laser beam is positioned on top of the edge ($x = x_0$), and the edge position is vibrating with a small amplitude u_x, the reflected light power is modulated at the same frequency and with an amplitude marked P_0 in Fig. 4.5. For small vibration amplitudes, the dependence of the measured P_0 on the in-plane vibration amplitude u_x can be assumed to be linear, $P_0 = ku_x$. The proportionality constant k is given by the slope of the power curve in Fig. 4.5, and hence is determined by the waist size w_0 and the maximum optical power reflected from the sample.

The in-plane detection response was simulated numerically for the two-dimensional (2D) case. The circular etch hole was described by a step function [**VI**] and the in-plane vibration by a vector $\mathbf{u} = (u_x, u_y)$, where u_x and u_y are the amplitudes of the vibration components along the x and y axes. The vibration amplitudes are assumed to be constant over the small area containing one etch hole. The intensity distribution of the Gaussian beam is [207]

$$I(r) = \frac{2P_l}{\pi w_0^2} \exp\left(\frac{-2r^2}{w_0^2}\right), \qquad (4.4)$$

where P_l is the optical power of the beam and r is the radial coordinate, i.e., $r^2 = x^2 + y^2$.

To simulate the measurement, the laser beam position was raster-scanned in two dimensions over a surface area containing one etch hole. At each scan point, the power of the reflected light was calculated by determining the overlap integral of the Gaussian beam profile and the reflecting plane surface containing the circular hole. It was assumed that any light falling in the hole is lost. The slope coefficient vector $\mathbf{k} = (k_x, k_y)$ at each scan point was then found by determining the gradient of the overlap integral. Finally, the modulation of the reflected optical power caused by the in-plane vibrations was obtained by taking the scalar product of $\mathbf{k}$ and $\mathbf{u}$.

Figure 4.6 shows a simulated response corresponding to an areal scan over an etch hole when the in-plane vibration is in 45° angle with respect to the x axis [$\mathbf{u} = (1, 1)$]. The diameter of the hole and the waist size of the Gaussian beam were set to 2 μm and 0.8 μm, respectively, corresponding to experimental values. The plot reveals information on both the amplitude and direction of the in-plane vibration. The signal peaks at points where the center of the laser beam coincides with the edge on opposite sides of the hole. Within the approximation of small vibrations, the signal strength at these maxima is directly proportional to the amplitude of the in-plane vibration. A straight line drawn through the maxima gives the direction of the vibration.

To estimate the minimum detectable amplitude of the in-plane vibration in one dimension, k and P_0 must be approximated. The slope coefficient k is obtained by calculating the derivative of Eq. (4.3) at $x = x_0$ and by multiplying this by P_{max}, the
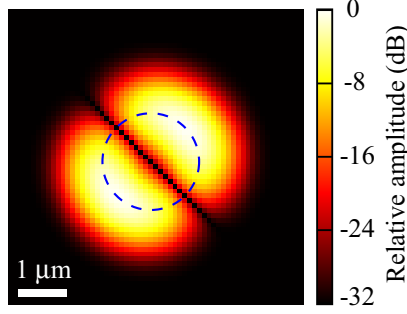
Figure 4.6: Simulated intensity-modulation data yielding the amplitude and direction of the in-plane vibration, which was set to $\mathbf{u} = (1,1)$ in this case. The dashed circle indicates the edge of the etch hole.

optical power at the high-speed photodetector when the laser beam is reflected from the silicon substrate,

$$k = -\sqrt{\frac{2}{\pi}} \frac{P_{max}}{w_0}. \tag{4.5}$$

The power P_0 can be approximated by using the electrical power measured by the spectrum analyzer. For this, it is assumed that the current i from the photodetector, being proportional to the optical power, is

$$i = i_{DC} + i_0 \sin(\omega_S t) = SP_{DC} + SP_0 \sin(\omega_S t), \tag{4.6}$$

where DC stands for direct current, $S = 0.28$ A/W is the responsivity of the photodetector and i_0 and P_0 are the amplitudes of the modulation signals. Since the photodetector is terminated with a load $R = 50\ \Omega$, the electrical power measured by the spectrum analyzer at the frequency $\omega_s/2\pi$ is

$$P_{SPA} = \frac{1}{2}GRi_0^2 = \frac{1}{2}GRS^2 P_0^2, \tag{4.7}$$

where $G = 26$ dB is the gain of the amplifier used before the spectrum analyzer. Using Eq. (4.7), we can estimate P_0 as a function of P_{SPA}, and hence we obtain

$$|u_x| = \left| \frac{P_0}{k} \right| = \sqrt{\frac{P_{SPA}}{GRS^2}} \sqrt{\frac{\pi}{2}} \frac{w_0}{P_{max}}. \tag{4.8}$$

Assuming P_{SPA} = -104 dBm (the noise floor of the detection electronics) and P_{max} = 0.4 mW, the minimum detectable amplitude of the in-plane vibration is $\sim$20 pm.

4.4 Results for the square-plate resonator

Vibration modes of the square plate MEMS resonator were analyzed by measuring both in- and out-of-plane vibrations using the setup described in Sections 2.2 and 4.3. The laser-probe measurements were conducted at several frequencies around the resonance frequencies of the Lamé and SE modes. The measurements were carried out both under ambient air pressure and in vacuum (pressure below 1 mbar). The resonator was electrically excited with a nominal input power of 0 dBm and with a bias voltage of 60 V.

Figure 4.7 shows the measured out-of-plane vibrations for three modes. The scans covering the complete resonator area were measured under ambient air pressure. Figure 4.7(a) depicts the measurement results at the resonance frequency of the SE mode, at 13.12 MHz. By comparing the measured vibration field to finite-element-method (FEM) simulations, it was concluded that the observed amplitude profile is a superposition of the out-of-plane component of the SE mode and that of a parasitic vertical mode [**VI**]. The scan in Fig. 4.7(b) was measured at the resonance frequency of the Lamé mode, at 12.16 MHz. The vibration profile is dominated by the parasitic vertical mode over the vanishing out-of-plane component of the Lamé mode. The scan in Fig. 4.7(c) shows the out-of-plane component of another parasitic mode. The measured amplitude profile matches well with the simulated profile [**VI**]. The measured profiles reveal vibrations also outside the resonator plate, i.e., in the anchor regions
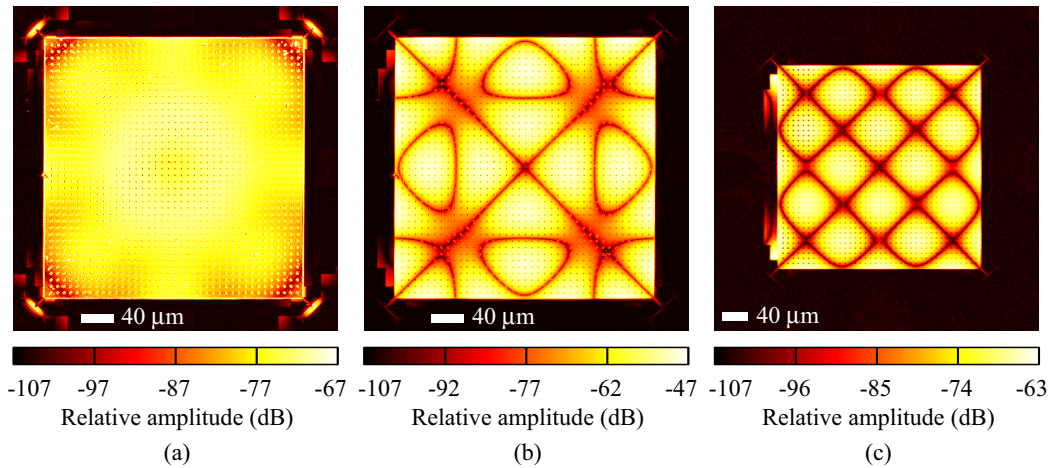

Figure 4.7: Out-of-plane vibrations in the MEMS resonator measured under ambient air pressure at the frequency of (a) the SE mode (13.106 MHz), (b) the Lamé mode (12.134 MHz), and (c) 10.927 MHz.

and around the ends of the input electrode. This indicates energy leakage from the resonator causing additional losses and hence decrease of the Q of the resonator.

In-plane vibrations were measured by detecting the intensity modulation of the reflected laser beam, as explained in Section 4.3. Figure 4.8 shows data measured under ambient air pressure at the resonance frequency of the SE mode. The amplitude of the in-plane vibration is obtained by searching for the two maxima of each spot pair. The direction of the vibration is given by a straight line drawn through the maxima of the two spots around each etch hole. Hence the in-plane vibration component of the SE mode can be obtained at discrete points, i.e., on top of each etch hole. The additional spots in between the grid of the etch holes are due to particles on the sample surface. The amplitude at the edges of the resonator plate and at the T-shaped anchors can also be seen in Fig. 4.8.
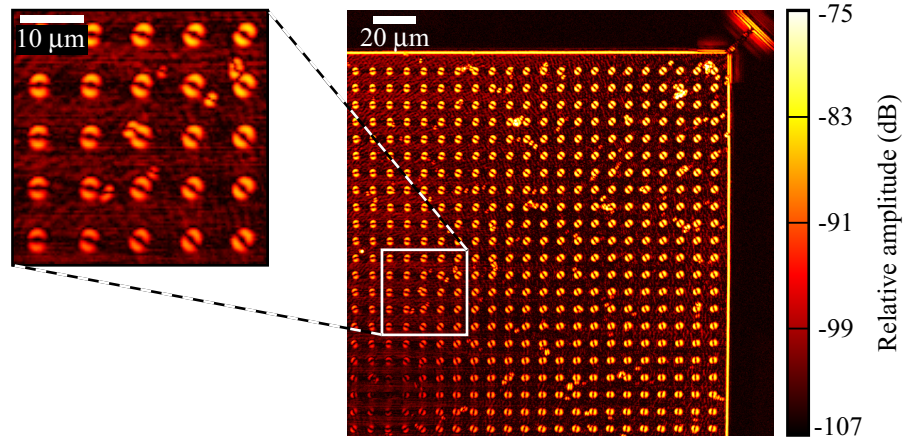
Figure 4.8: Optical intensity modulation data yielding the relative amplitude of the in-plane vibrations in the upper-right quarter of the resonator plate. The measurement is carried out under ambient air pressure at the frequency of the SE mode (13.106 MHz).

The measured in-plane vibrations can be presented as a vector field. The vectors extracted from the intensity-modulation data are drawn on top of the etch holes. The orientation and the length of each vector are calculated by determining the positions and maximum values of the two spots around each etch hole. The in-plane vibrations of the SE and Lamé modes measured in the upper-right quarter of the resonator plate are shown in Figs. 4.9(a) and 4.9(b), respectively. The vector field of the SE mode shows radial behavior whereas that of the Lamé mode oscillates through the diagonal and is perpendicular at the edges of the plate.
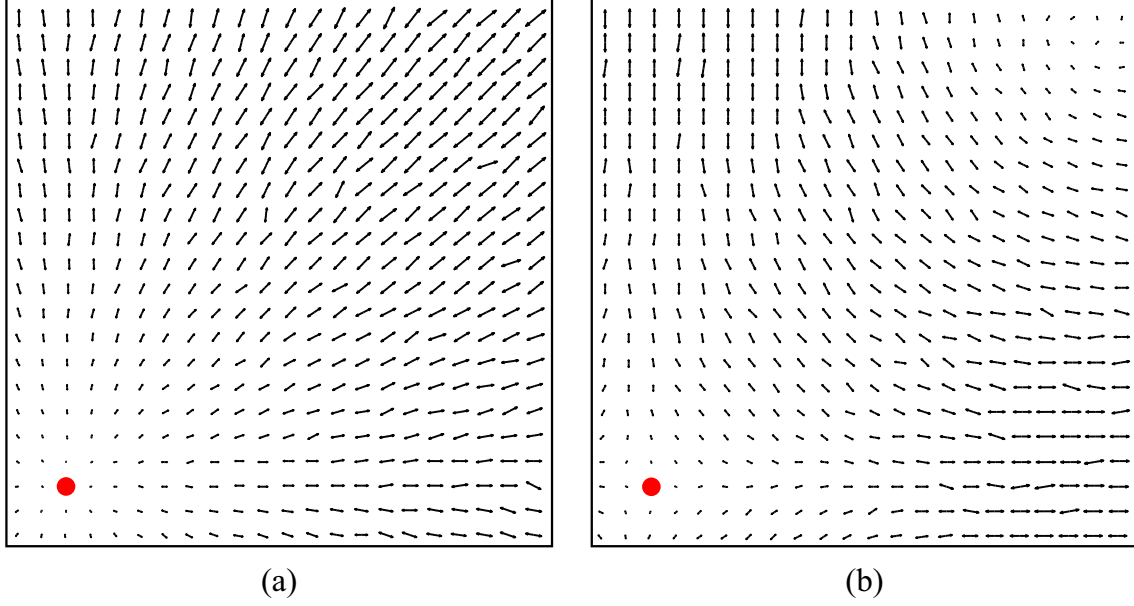
Figure 4.9: Vector fields of the in-plane vibrations measured under ambient air pressure for (a) the SE mode (13.106 MHz), and (b) the Lamé mode (12.134 MHz) in the upper-right quarter of the resonator. The center of the resonator plate is indicated with a dot. The measured vibration fields match the mode behavior illustrated in Fig. 4.2.

In order to determine the mechanical frequency responses and the associated Q values of the Lamé and SE modes, scans with high spatial resolution were carried out at several frequencies. Small scan areas containing one or two etch holes were chosen to minimize the scanning time and thus to eliminate possible drift of the resonance frequencies, for example, due to temperature variations. The use of a fixed scanning location is justified since the mode shapes of the vibration fields do not change in the narrow frequency range studied. Both the out-of-plane and in-plane vibrations were studied.

After extracting the mechanical frequency response from the measurement data, the theoretical response given by Eq. (4.2) was fitted to the experimental data. The equation was transformed to logarithmic scale with an expression $20 \log_{10}(|X|) + A$. The fit parameters are the resonance frequency $f_0 = \omega_0/2\pi$, quality factor Q, parameter F/K and the offset A.

Figure 4.10 depicts the mechanical frequency response measured around the resonance frequency of the SE mode. The theoretical curve fits well to the experimental

Figure 4.10: Mechanical frequency responses measured at the frequency of the SE mode: (a) out-of-plane vibrations and (b) in-plane vibrations.

data for all the four cases: the in-plane and the out-of-plane vibrations measured both under ambient air pressure and in vacuum. When the pressure is lowered from the ambient air pressure to vacuum, the resonance frequencies decrease approximately by 3.4 kHz while the maximum amplitudes increase by 18 dB. Also, the Q values in vacuum are about nine times the ones measured under ambient air pressure. It should be noted that the relative amplitude values measured for the in-plane and out-of-plane vibrations cannot be compared to each other due to differences in the detection principles.

Figure 4.11 shows the mechanical frequency response measured around the resonance frequency of the Lamé mode. In the responses, two resonance peaks exist with a small frequency separation. This becomes evident in the vacuum measurements, where the higher Q leads to a clear separation of the two resonance peaks. The frequency difference between these two peaks is 3 kHz, which corresponds to that observed in the electrical measurements, see Fig. 4.3. The amplitude fields of the out-of-plane vibrations measured in vacuum at 12.131 MHz and 12.134 MHz appear identical with the amplitude profile shown in Fig. 4.7(b). The corresponding in-plane vibrations are similar to those shown in Fig. 4.9(b). The fitted curves of the out-of-plane component in Fig. 4.11(a) were obtained by fitting a sum of two separate theoretical responses, described by Eq. (4.2). The same applies to the in-plane component measured in vacuum, Fig. 4.11(b). For the in-plane component measured under ambient air pressure, see Fig. 4.11(b), a single theoretical response curve fits well the experimental data.
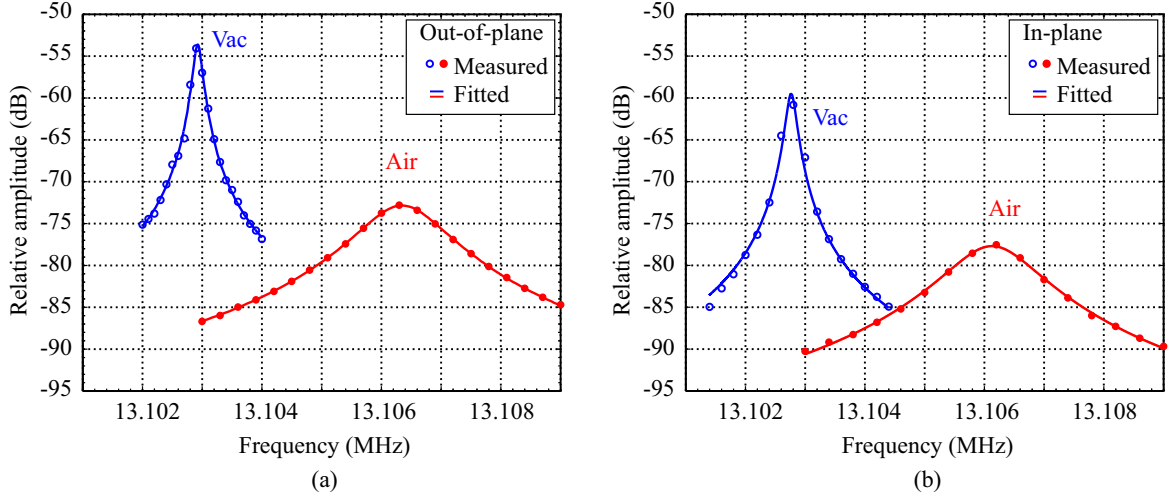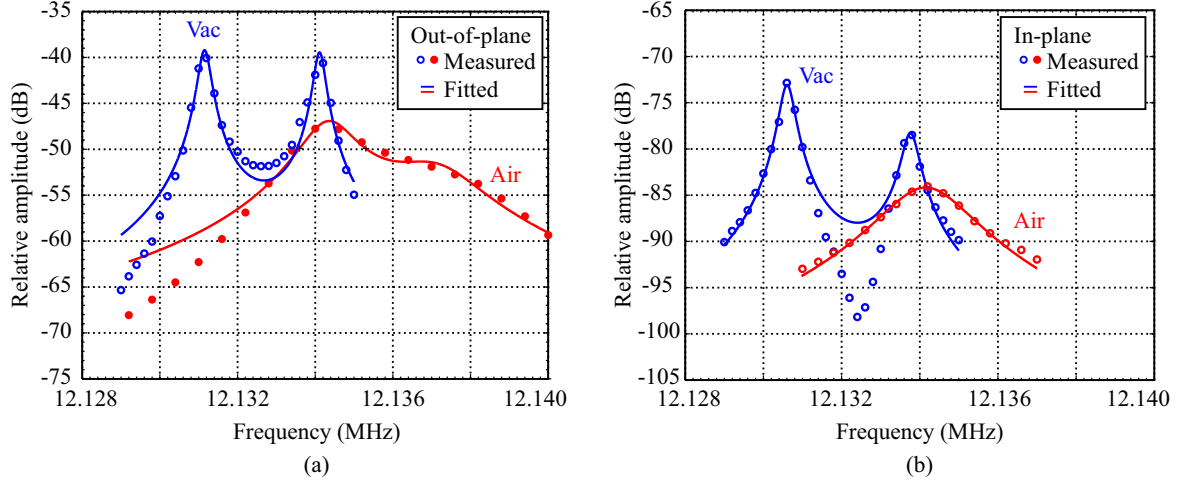
Figure 4.11: Mechanical frequency responses measured at the frequency of the Lamé mode: (a) out-of-plane vibrations and (b) in-plane vibrations.

The Q values of the SE and Lamé modes were obtained from the fits of the theoretical responses to the experimental data. Table I summarizes the Q values as averages over five measurement sets together with the Q values calculated from the electrical measurements. The values for the in- and out-of-plane vibrations are approximately the same and match well with the Q values obtained from the electrical measurements. The standard deviation of the resonance frequency in the five measurement sets is about 0.1 kHz in each case. The standard deviations of the extracted Q values in ambient air pressure and in vacuum are ~ 1 % and ~ 10 %, respectively. There is, however, one exception: the standard deviation for the Q value of the in-plane vibration of the SE mode measured in vacuum is 25 %. This could be explained by the combination of a finite scan step and drift of the sample position causing an error in the extracted vibration amplitude. It should also be noted that for the out-of-plane response of the Lamé mode in ambient air pressure, the simple model does not fit as nicely as for the other cases.

It is also interesting to compare the simulated and measured resonance frequencies, see Publication [**VI**]. According to the FEM simulations, the resonance frequencies of the vertical modes should differ from the resonance frequencies of the in-plane modes (SE and Lamé modes). Based on the laser-probe measurements, however, it seems that the measured in- and out-of-plane vibrations feature about the same resonance frequencies and roughly the same Q values. This could be explained by assuming that the in- and out-of-plane vibration modes are coupled and the out-of-plane vibration

mode is excited by the in-plane mode. On the other hand, the difference between the simulated and measured resonance frequencies could also be explained by the fact that the etch holes and the anchor springs were not included in the simulations.

Table I: Q values determined from the out-of-plane and in-plane vibration measurements, and from the electrical responses.

Mode	Out-of-plane	In-plane	Electrical
SE, air	9500	8900	9900
SE, vac	89000	65000	87000
Lamé, air	8600/5300	5500	6100
Lamé, vac	36000/31000	34000/26000	37000

5 Conclusion

The dissertation focuses on measuring and analyzing vibration fields in SAW and MEMS devices using the scanning Michelson laser interferometer developed at TKK. The interferometer as such detects out-of-plane vibrations, i.e., vibrations perpendicular to the surface of the device. In the thesis, a novel detection method to measure also in-plane vibrations is presented. The method is based on detecting the intensity modulation of the laser beam reflected from the edges of the release etch holes on the surface of a MEMS resonator. Other contrast features on the sample surface can as well be employed to obtain information of the in-plane vibrations.

The laser-probe measurements enable direct studies of the vibration fields in SAW and MEMS devices and hence provide new information on their physics and operation not obtainable from electrical measurements alone. Moreover, by comparing the results of laser-probe and electrical measurements to numerical simulations, the operation of microacoustic devices can be analyzed thoroughly. Such analyses provide significant support for the research and development of new SAW and MEMS components satisfying stringent specifications.

In the first part of the thesis, operation of novel SAW devices, such as LLSAW resonator, double resonance filter and R-SPUDT filter with transverse mode suppression was thoroughly analyzed by comparing the interferometric measurement results to numerical simulations and data from electrical measurements. The measurements of the vibration fields in the LLSAW resonator revealed side radiation of Rayleigh waves, which constitutes an acoustic loss mechanism for the resonator. The measurements of the double resonance filter confirmed the operation principle of the device, and in particular, the fact that a considerable part of the acoustic energy is concentrated in the gap area at the hiccup resonance frequency. This may limit the power handling capability of the filter. The analysis of the R-SPUDT filter indicated that one of the parameters for the transverse mode suppression had been underestimated in the filter design.

In the second part of the thesis, vibration modes in a square-plate MEMS resonator were analyzed. Comparing the laser-probe measurements with simulations, it could be concluded that the main in-plane vibration mode is companioned by a parasitic out-of-plane mode, which may affect the quality factor of the main resonance. The measurements also revealed vibration amplitudes outside the resonator plate, i.e., in the anchor regions and around the ends of the input electrode. These additional vibrations indicate energy leakage from the resonator causing additional losses.

The cases studied in this thesis serve to demonstrate the diverse capabilities of laser-

probe measurements in the research of microacoustic devices. In particular, when such measurements are combined with the data obtained from electrical measurements and numerical simulations, extremely detailed information on the operation of the devices may be obtained. This information has turned out to be of great practical value in the research and development of SAW and MEMS devices in industrial scale. Based on the experience gained during this work, one can conclude that there will be increased demand for laser probing of electroacoustic devices in the future.

References

[1] R. Weigel, D. P. Morgan, J. M. Owens, A. Ballato, K. M. Lakin, K.-Y. Hashimoto, and C. C. W. Ruppel, "Microwave acoustic materials, devices, and applications", *IEEE Trans. Microwave Theory Tech.* **50**, pp. 738–749 (2002).

[2] D. P. Morgan, "History of saw devices", in *Proc. IEEE Int. Freq. Contr. Symp.*, pp. 439–460 (1998).

[3] P. Hariharan, *Basics of Interferometry.* San Diego: Academic Press, 1992.

[4] A. A. Michelson, "The relative motion of the earth and the luminiferous ether", *Amer. J. Sci.* **22**, pp. 120–129 (1881).

[5] A. A. Michelson, "Interference phenomena in a new form of refractometer", *Phil. Mag.* **13**, pp. 236–242 (1882).

[6] J. V. Knuuttila, P. T. Tikka, and M. M. Salomaa, "Scanning Michelson interferometer for imaging surface acoustic wave fields", *Opt. Lett.* **25**, pp. 613–615 (2000).

[7] G. Arfken, *Mathematical Methods for Physicists*, 4th ed. San Diego: Academic Press, 1995.

[8] S. Sääskilahti, "Pinta-akustisten aaltojen optinen kuvantaminen", Master's thesis, Materials Physics Laboratory, Helsinki University of Technology, Espoo, August 1996, in Finnish.

[9] J. Knuuttila, "Advanced interferometric imaging system for surface acoustic waves", Master's thesis, Materials Physics Laboratory, Helsinki University of Technology, Espoo, September 1998.

[10] J. M. Khosrofian and B. A. Garetz, "Measurement of a Gaussian laser beam diameter through the direct inversion of knife-edge data", *Appl. Opt.* **22**, pp. 3406–3410 (1983).

[11] T. Makkonen, T. Pensala, J. Vartiainen, J. V. Knuuttila, J. Kaitila, and M. M. Salomaa, "Estimating materials parameters in thin-film BAW resonators using measured dispersion curves", *IEEE Trans. Ultrason., Ferroelect., Freq. Contr.* **51**, pp. 42–51 (2004).

[12] A. Gollwitzer, A. Lerner, and G. Fischerauer, "Interferometric observation of surface acoustic wave phase fronts", in *Proc. IEEE Int. Freq. Cont. Symp.*, pp. 424–427 (2006).

[13] L. Lipiäinen, K. Kokkonen, O. Holmgren, and M. Kaivola, "Method for phase sensitive measurements of surface vibrations using homodyne interferometry without stabilization", in *Proc. IEEE Ultrasonics Symposium*, accepted (2009).

[14] Lord Rayleigh, "On waves propagating along the plane surface of an elastic solid", in *Proc. London Math. Soc.*, **7**, pp. 4–11 (1885).

[15] "IEEE standard on piezoelectricity", ANSI/IEEE Std 176-1987, New York, 1988.

[16] K. Hashimoto, *Surface Acoustic Wave Devices in Telecommunications.* Berlin: Springer-Verlag, 2000.

[17] R. M. White and F. W. Voltmer, "Direct piezoelectric coupling to surface elastic waves", *Appl. Phys. Lett.* **17**, pp. 314–316 (1965).

[18] D. P. Morgan, *Surface-Wave Devices for Signal Processing.* Amsterdam: Elsevier, 1991.

[19] C. S. Hartmann, P. V. Wright, R. J. Kansy, and E. M. Garber, "An analysis of SAW inter-digital transducers with internal reflections and the application to the design of single-phase unidirectional transducer", in *Proc. IEEE Ultrasonics Symposium*, pp. 40–45 (1982).

[20] P. V. Wright and S. A. Wilkus, "A prototype low-loss filter employing single-phase unidirectional transducers", in *Proc. IEEE Ultrasonics Symposium*, pp. 72–76 (1983).

[21] T. Kodama, H. Kawabata, Y. Yashuhara, and H. Sato, "Design of low-loss SAW filters employing distributed acoustic reflection transducers", in *Proc. IEEE Ultrasonics Symposium*, pp. 59–64 (1986).

[22] C. S. Hartmann and B. P. Abbott, "Overview of design challenges for single phase unidirectional SAW filters", in *Proc. IEEE Ultrasonics Symposium*, pp. 79–89 (1989).

[23] P. Ventura, M. Solal, P. Dufilie, J. M. Hode, and F. Roux, "A new concept in SPUDT design: the RSPUDT (resonant SPUDT)", in *Proc. IEEE Ultrasonics Symposium*, pp. 1–6 (1994).

[24] M. A. Sharif, C. Lambert, D. P. Chen, and C. S. Hartmann, "Network coupled, high performance SAW resonator filters", in *Proc. IEEE Ultrasonics Symposium*, pp. 135–138 (1994).

[25] M. A. Sharif, M. A. Schwab, D. P. Chen, and C. S. Hartmann, "Coupled resonator filters with differential input and/or differential output", in *Proc. IEEE Ultrasonics Symposium*, pp. 67–70 (1995).

[26] T. Morita, Y. Watanabe, M. Tanaka, and Y. Nakazawa, "Wideband low loss douple mode SAW filters", in *Proc. IEEE Ultrasonics Symposium*, pp. 95–104 (1992).

[27] S. Ichikawa, H. Kanasaki, N. Akahori, M. Koshino, and Y. Ebata, "Mode analysis of longitudinal multi mode SAW resonator filter", in *Proc. IEEE Ultrasonics Symposium*, pp. 101–106 (2001).

[28] O. Ikata, T. Miyashita, T. Matsuda, T. Nishihara, and Y. Satoh, "Development of low-loss band-pass filters using SAW resonators for portable telephones", in *Proc. IEEE Ultrasonics Symposium*, pp. 111–115 (1992).

[29] L. Espenschied, "Electrical wave filter", U.S. patent 1,795,204, 1931.

[30] S. Lehtonen, J. Koskela, M. M. Salomaa, V. P. Plessky, M. Honkanen, and J. Turunen, "Surface acoustic wave impedance element filters for 5 GHz", *Appl. Phys. Lett.* **75**, pp. 142–144 (1999).

[31] H. Odagawa and K. Yamanouchi, "10 GHz range extremely low-loss surface acoustic wave filter", *Electron. Lett.* **34**, pp. 865–866 (1998).

[32] A. A. R. Elshabini-Riad and F. D. Barlow III, *Thin film technology handbook.* McGraw-Hill, New York, 1998.

[33] V. I. Grigorievski, "Fast leaky surface acoustic waves on lithium niobate and lithium tantalate", in *Proc. IEEE Ultrasonics Symposium*, pp. 259–262 (2000).

[34] A. Isobe, M. Hikita, and K. Asai, "Propagation characteristics of longitudinal leaky SAW in Al-grating structure", *IEEE Trans. Ultrason., Ferroelect., Freq. Contr.* **46**, pp. 849–855 (1999).

[35] T. Makkonen, V. P. Plessky, W. Steichen, S. Chamaly, C. Poirel, M. Solal, and M. M. Salomaa, "Fundamental mode 5 GHz surface-acoustic-wave filters using optical lithography", *Appl. Phys. Lett.* **83**, pp. 3596–3598 (2003).

[36] T. Makkonen, V. P. Plessky, W. Steichen, M. S. V. I. Grigorievski, and M. M. Salomaa, "Longitudinal leaky SAW resonators and filters on YZ-LiNbO$_3$", *IEEE Trans. Ultrason., Ferroelect., Freq. Contr.* **53**, pp. 393–401 (2006).

[37] T. Makkonen, V. P. Plessky, W. Steichen, and M. M. Salomaa, "Surface-acoustic-wave devices for the 2.5–5 GHz frequency range based on longitudinal leaky waves", *Appl. Phys. Lett.* **82**, pp. 3351–3353 (2003).

[38] E. P. Ippen, "Diffraction of light by surface acoustic waves", *Proc. IEEE* **55**, pp. 248–249 (1967).

[39] A. Korpel, L. J. Laub, and H. C. Sievering, "Measurement of acoustic surface wave propagation characteristics by reflected light", *Appl. Phys. Lett.* **10**, pp. 295–297 (1967).

[40] J. Krokstad and L. O. Svaasand, "Scattering of light by ultrasonic surface waves in quartz", *Appl. Phys. Lett.* **11**, pp. 155–157 (1967).

[41] W. G. Mayer, G. B. Lamers, and D. C. Auth, "Interaction of light and ultrasonic surface waves", *J. Acoust. Soc. Amer.* **42**, pp. 1255–1257 (1967).

[42] D. C. Auth and W. G. Mayer, "Scattering of light reflected from acoustic surface waves in isotropic solids", *J. Appl. Phys.* **38**, pp. 5138–5140 (1967).

[43] R. Adler, A. Korpel, and P. Desmares, "An instrument for making surface waves visible", *IEEE Trans. Sonics, Ultrason.* **SU-15**, pp. 157–161 (1968).

[44] R. L. Whitman, L. J. Laub, and W. J. Bates, "Acoustic surface displacement measurements on a wedge-shaped transducer using an optical probe technique", *IEEE Trans. Sonics, Ultrason.* **SU-15**, pp. 186–189 (1968).

[45] R. L. Whitman and A. Korpel, "Probing of acoustic surface perturbations by coherent light", *Appl. Opt.* **8**, pp. 1567–1576 (1969).

[46] R. M. De La Rue, R. F. Humphryes, I. M. Mason, and E. A. Ash, "Acoustic-surface-wave amplitude and phase measurements using laser probes", in *Proc. of the IEE*, **119**, 2, pp. 117–126 (1972).

[47] G. I. Stegeman, "Optical probing of surface waves and surface wave devices", *IEEE Trans. Sonics, Ultrason.* **SU-23**, pp. 33–63 (1976).

[48] J. P. Monchalin, "Optical detection of ultrasound", *IEEE Trans. Ultrason., Ferroelect., Freq. Contr.* **33**, pp. 485–499 (1986).

[49] J. W. Wagner, "Optical detection of ultrasound", *Physical Acoustics* **XIX**, pp. 201–266 (1990).

[50] C. B. Scruby and L. E. Drain, *Laser Ultrasonics, Techniques and Applications.* Bristol: Adam Hilger, 1990.

[51] D. Royer and E. Dieulesaint, *Elastic Waves in Solids II.* Berlin: Springer-Verlag, 2000, pp. 157–233.

[52] J. V. Knuuttila, "Laser-interferometric analysis of surface acoustic wave resonators", Ph.D. dissertation, Helsinki University of Technology, Espoo, Finland, 2005.

[53] J. E. Graebner, B. P. Barber, P. L. Gammel, D. S. Greywall, and S. Gopani, "Dynamic visualization of subangstrom high-frequency surface vibrations", *Appl. Phys. Lett.* **78**, pp. 159–161 (2001).

[54] G. G. Fattinger and P. T. Tikka, "Modified Mach-Zehnder laser interferometer for probing bulk acoustic waves", *Appl. Phys. Lett.* **79**, pp. 290–292 (2001).

[55] H. Martinussen, A. Aksnes, and H. E. Engan, "High sensitivity vibration measurements with absolute calibration", in *Conf. IEEE CLEO/QELS*, pp. 1–2 (2006).

[56] K. Hashimoto, K. Kashiwa, T. Omori, M. Yamaguchi, O. Takano, S. Meguro, and K. Akahane, "A fast scanning laser probe based on Sagnac interferometer for RF surface and bulk acoustic wave devices", in *IEEE MTT-S Digest*, pp. 851–854 (2008).

[57] T. Tachizaki, T. Muroya, O. Matsuda, Y. Sugawara, D. H. Hurley, and O. B. Wright, "Scanning ultrafast Sagnac interferometry for imaging two-dimensional surface wave propagation", *Rev. Sci. Instrum.* **77**, p. 043713 (2006).

[58] D. M. Profunser, O. B. Wright, and O. Matsuda, "Imaging ripples on phononic crystals reveals acoustic band structure and Bloch harmonics", *Phys. Rev. Lett.* **97**, p. 55502 (2006).

[59] H. Yatsuda, S. Kamiseki, and T. Chiba, "Calculation and optical measurement of SAW diffraction pattern of slanted finger SAW filters on YZ LiNbO$_3$ and 128YX LiNbO$_3$", in *Proc. IEEE Ultrasonics Symposium*, pp. 13–17 (2001).

[60] T. Chiba, "Optical measurement and numerical analysis of SAW propagation at dispersive delay line on Y-Z LiNbO$_3$ substrate", in *Proc. IEEE Ultrasonics Symposium*, pp. 1718–1721 (2003).

[61] T. Chiba, "Amplitude and phase measurement of surface acoustic waves within a SAW filter having fan-shaped transducers and numerical simulations", in *Proc. IEEE Ultrasonics Symposium*, pp. 1584–1587 (2005).

[62] K. Kokkonen, J. V. Knuuttila, V. P. Plessky, and M. M. Salomaa, "Phase-sensitive absolute-amplitude measurements of surface waves using heterodyne interferometry", in *Proc. IEEE Ultrasonics Symposium*, pp. 1145–1148 (2003).

[63] K. Kokkonen and M. Kaivola, "Scanning heterodyne laser interferometer for phase-sensitive absolute-amplitude measurements of surface vibrations", *Appl. Phys. Lett.* **92**, p. 063502 (2008).

[64] S. Sääskilahti, J. Knuuttila, M. Kaivola, C. G. Aminoff, and M. M. Salomaa, "Interferometric investigation of SAW devices", in *Proc. IEEE Ultrasonics Symposium*, pp. 173–176 (1996).

[65] J. Koskela, "Analysis and modeling of surface-acoustic wave resonators", Ph.D. dissertation, Helsinki University of Technology, Espoo, Finland, 2000.

[66] T. Makkonen, "Numerical simulations of microacoustic resonators and filters", Ph.D. dissertation, Helsinki University of Technology, Espoo, Finland, 2005.

[67] K. Kokkonen, M. Kaivola, S. Benchabane, A. Khelif, and V. Laude, "Scattering of surface acoustic waves by a phononic crystal revealed by heterodyne interferometry", *Appl. Phys. Lett.* **91**, p. 083517 (2007).

[68] H. E. Engan, "Phase sensitive laser probe for high-frequency surface acoustic wave measurements", *IEEE Trans. Sonics, Ultrason.* **SU-25**, pp. 372–377 (1978).

[69] H. E. Engan, "A phase sensitive laser probe for pulsed saw measurements", *IEEE Trans. Sonics, Ultrason.* **SU-29**, pp. 281–283 (1982).

[70] G. Sölkner, A. Ginter, and H.-P. Grassl, "Phase-preserving imaging of high frequency surface acoustic wave fields", *Mater. Sci. Eng.* **A122**, pp. 43–46 (1989).

[71] A. Ginter and G. Sölkner, "Phase accurate optical probing of surface acoustic wave devices", *Appl. Phys. Lett.* **56**, pp. 2295–2297 (1990).

[72] P. Kessler, G. Sölkner, and K. C. Wagner, "Imaging of the wave field of surface acoustic wave devices", in *Proc. IEEE Ultrasonics Symposium*, pp. 27–30 (1991).

[73] A. Holm, R. Weigel, P. Russer, and W. Ruile, "A laser probing system for characterization of SAW propagation on LiNbO$_3$, LiTaO$_3$, and quartz", in *IEEE MTT-S Digest*, pp. 1541–1544 (1996).

[74] S. Jen and C. S. Hartmann, "Recent advances in SAW laser probe", in *Proc. IEEE Ultrasonics Symposium*, pp. 33–36 (1996).

[75] A. Holm, P. Wallner, W. Ruile, and R. Weigel, "High-resolution optical probing of SAW and leaky SAW structures", in *Proc. IEEE Ultrasonics Symposium*, pp. 153–156 (1997).

[76] H. E. Engan and A. Rønnekleiv, "Enhancement of SAW laser probe measurements by signal processing", in *Proc. IEEE Ultrasonics Symposium*, pp. 217–220 (1999).

[77] S. Rooth, S. Bardal, T. Viken, Ø. Johansen, and E. Halvorsen, "Laserprobe measurements of SAWs at 3 GHz on a free surface of rotated Y-cut quartz", in *Proc. IEEE Ultrasonics Symposium*, pp. 201–205 (2001).

[78] H. Kamizuma, T. Omori, K. Hashimoto, and M. Yamaguchi, "Development of fast-scanning laser probe system based on knife-edge method for diagnosis of RF surface acoustic wave devices", *IEEE Trans. Ultrason., Ferroelect., Freq. Contr.* **53**, pp. 1186–1191 (2006).

[79] K. Hashimoto, H. Kamizuma, M. Watanabe, T. Omori, and M. Yamaguchi, "Wavenumber domain analysis of two-dimensional SAW images captured by phase-sensitive laser probe system", *IEEE Trans. Ultrason., Ferroelect., Freq. Contr.* **54**, pp. 1072–1075 (2007).

[80] K. L. Telschow, V. A. Deason, D. L. Cottle, and I. J. D. Larson, "Full-field imaging of gigahertz film bulk acoustic resonator motion", *IEEE Trans. Ultrason., Ferroelect., Freq. Contr.* **50**, pp. 1279–1285 (2003).

[81] Y. Watanabe, T. Sato, S. Goka, and H. Sekimoto, "Non-scanning means for determining vibrational distribution in BAW and SAW devices", in *Proc. IEEE Ultrasonics Symposium*, pp. 953–956 (2002).

[82] C. Bödefeld, F. Beil, H. J. Kutschera, M. Streibl, and A. Wixforth, "Imaging of surface acoustic waves", in *Proc. IEEE Ultrasonics Symposium*, pp. 145–148 (2001).

[83] P. V. Santos, "Acoustic field mapping on GaAs using microscopic reflectance and reflectance anisotropy", *Appl. Phys. Lett.* **74**, pp. 4002–4004 (1999).

[84] A. Miyamoto, S. Wakana, and A. Ito, "Novel optical observation technique for shear horizontal wave in SAW resonators on 42°YX-cut lithium tantalate", in *Proc. IEEE Ultrasonics Symposium*, pp. 89–92 (2002).

[85] S. Wakana, A. Miyamoto, and A. Ito, "Backside observation technique for SAW distribution under electrodes", in *Proc. IEEE Ultrasonics Symposium*, pp. 1714–1717 (2003).

[86] S. Matsuda, A. Miyamoto, S. Wakana, and A. Ito, "Observation of waves propagating within a substrate", in *Proc. IEEE Ultrasonics Symposium*, pp. 1876–1879 (2004).

[87] E. Chilla, T. Hesjedal, and H.-J. Fröhlich, "Nanoscale determination of phase velocity by scanning acoustic force microscopy", *Phys. Rev. B* **55**, pp. 15 852–15 855 (1997).

[88] T. Hesjedal, E. Chilla, and H. J. Fröhlich, "High resolution visualization of acoustic wave fields within surface acoustic wave devices", *Appl. Phys. Lett.* **70**, pp. 1372–1374 (1997).

[89] G. Behme, T. Hesjedal, E. Chilla, and H. J. Fröhlich, "Transverse surface acoustic wave detection by scanning acoustic force microscopy", *Appl. Phys. Lett.* **73**, pp. 882–884 (1998).

[90] T. Hesjedal and G. Behme, "Investigation of single surface acoustic wave sources", *Electron. Lett.* **36**, pp. 1903–1904 (2000).

[91] T. Hesjedal and G. Behme, "High-resolution imaging of surface acoustic wave scattering", *Appl. Phys. Lett.* **78**, pp. 1948–1950 (2001).

[92] T. Hesjedal and G. Behme, "High-resolution imaging of a single circular surface acoustic wave source: Effects of crystal anisotropy", *Appl. Phys. Lett.* **79**, pp. 1054–1056 (2001).

[93] T. Hesjedal and G. Behme, "AFM observation of surface acoustic waves emitted from singlesymmetric SAW transducers", *IEEE Trans. Ultrason., Ferroelect., Freq. Contr.* **48**, pp. 641–642 (2001).

[94] G. Behme and T. Hesjedal, "Investigation of crossed SAW fields by scanning acoustic force microscopy", *IEEE Trans. Ultrason., Ferroelect., Freq. Contr.* **48**, pp. 1132–1138 (2001).

[95] T. Hesjedal, J. Mohanty, F. Kubat, W. Ruile, and L. M. Reindl, "A microscopic view on acoustomigration", *IEEE Trans. Ultrason., Ferroelect., Freq. Contr.* **52**, pp. 1584–1593 (2005).

[96] E. Chilla and H.-J. Fröhnlich, "Investigation of surface acoustic wave fields by scanning tunneling microscopy", in *Proc. IEEE Ultrasonics Symposium*, pp. 355–362 (1994).

[97] W. J. Tanski and N. D. Wittels, "SEM observations of SAW resonator transverse modes", *Appl. Phys. Lett.* **34**, pp. 537–539 (1979).

[98] G. Eberharter and H. P. Feuerbaum, "Scanning-electron-microscope observations of propagating acoustic waves in surface acoustic wave devices", *Appl. Phys. Lett.* **37**, pp. 698–699 (1980).

[99] D. V. Roshchupkin and M. Brunel, "Scanning electron microscopy observation of surface acoustic wave propagation in the LiNbO$_3$ crystals with regular domain structures", *IEEE Trans. Ultrason., Ferroelect., Freq. Contr.* **41**, pp. 512–517 (1994).

[100] S. A. Sakharov, O. A. Buzanov, and D. V. Roshchupkin, "Investigation of SAW and PSAW propagation in LGS crystal by scanning electron microscopy method", in *Proc. IEEE Int. Freq. Contr. Symp.*, pp. 698–700 (2003).

[101] R. W. Whatmore, P. A. Goddard, and B. K. Tanner, "Stroboscopic X-ray topography of surface acoustic wave devices", in *Proc. IEEE Ultrasonics Symposium*, pp. 363–366 (1982).

[102] A. Zarka, B. Capelle, M. Pilard, J. Detaint, and M. Solal, "An analysis of the S.A.W. displacements in quartz and lithium niobate by X-ray topography", in *Proc. IEEE Ultrasonics Symposium*, pp. 705–708 (1994).

[103] E. Zolotoyabko, D. Shilo, W. Sauer, E. Pernot, and J. Baruchel, "Stroboscopic x-ray topography in crystals under 10-μm-surface acoustic wave excitation", *Rev. Sci. Instrum.* **70**, p. 3341 (1999).

[104] W. Sauer, M. Streibl, T. H. Metzger, A. G. C. Haubrich, S. Manus, A. Wixforth, J. Peisl, A. Mazuelas, J. Haertwig, and J. Baruchel, "Imaging surface acoustic waves on GaAs by X-ray diffraction techniques", in *Proc. IEEE Ultrasonics Symposium*, pp. 69–72 (1999).

[105] D. V. Roshchupkin, H. D. Roshchupkina, and D. V. Irzhak, "X-ray topography analysis of acoustic wave fields in the SAW-resonator structures", *IEEE Trans. Ultrason., Ferroelect., Freq. Contr.* **52**, pp. 2081–2087 (2005).

[106] R. Tucoulou, M. Brunel, D. V. Roshchupkin, I. A. Schelokov, J. Colin, and J. Grilhé, "Electro-migration in al thin films induced by surface acoustic waves: Application to imaging", *IEEE Trans. Ultrason., Ferroelect., Freq. Contr.* **46**, pp. 856–860 (1999).

[107] M. K. Tan, J. R. Friend, and L. Y. Yeo, "Direct visualization of surface acoustic waves along substrates using smoke particles", *Appl. Phys. Lett.* **91**, p. 224101 (2007).

[108] H. Safar, R. N. Kleiman, B. P. Barber, P. L. Gammel, J. Pastalan, H. Huggins, L. Fetter, and R. Miller, "Imaging of acoustic fields in bulk acoustic-wave thin-film resonators", *Appl. Phys. Lett.* **77**, pp. 136–138 (2000).

[109] O. Kawachi, S. Mineyoshi, G. Endoh, M. Ueda, O. Ikata, K. Hashimoto, and M. Yamaguchi, "Optimal cut for leaky SAW on LiTaO$_3$ for high performance resonators and filters", *IEEE Trans. Ultrason., Ferroelect., Freq. Contr.* **48**, pp. 1442–1448 (2001).

[110] K. Hashimoto, M. Yamaguchi, G. Kovacs, K. C. Wagner, W. Ruile, and R. Weigel, "Effects of bulk wave radiation on IDT admittance on 42°YX-LiTaO$_3$", *IEEE Trans. Ultrason., Ferroelect., Freq. Contr.* **48**, pp. 1419–1425 (2001).

[111] J. V. Knuuttila, J. Saarinen, C. S. Hartmann, V. P. Plessky, and M. M. Salomaa, "Measurement of BAW radiation from low-loss LSAW resonators", *Electron. Lett.* **37**, pp. 1055–1056 (2001).

[112] J. V. Knuuttila, J. J. Vartiainen, J. Koskela, V. P. Plessky, C. S. Hartmann, and M. M. Salomaa, "Bulk-acoustic waves radiated from low-loss surface-acoustic-wave resonators", *Appl. Phys. Lett.* **84**, pp. 1579–1581 (2004).

[113] J. V. Knuuttila, P. T. Tikka, C. S. Hartmann, V. P. Plessky, and M. M. Salomaa, "Anomalous asymmetric acoustic radiation in low-loss SAW filters", *Electron. Lett.* **35**, pp. 1115–1116 (1999).

[114] J. Koskela, J. V. Knuuttila, P. T. Tikka, C. S. Hartmann, V. P. Plessky, and M. M. Salomaa, "Mechanism for acoustic leakage in surface-acoustic wave resonators on rotated Y-cut lithium tantalate substrate", *Appl. Phys. Lett.* **75**, pp. 2683–2685 (1999).

[115] T. Shiba, S. Oosawa, J. Hamasaki, Y. Fujita, and T. Chiba, "Low loss SAW double-mode structure suppressing spurious radiation", in *Proc. IEEE Ultrasonics Symposium*, pp. 2008–2011 (2004).

[116] J. Koskela, J. V. Knuuttila, T. Makkonen, V. P. Plessky, and M. M. Salomaa, "Acoustic loss mechanisms in leaky SAW resonators on lithium tantalate", *IEEE Trans. Ultrason., Ferroelect., Freq. Contr.* **48**, pp. 1517–1526 (2001).

[117] S. V. Biryukov, Y. V. Gulyaev, V. V. Krylov, and V. P. Plessky, *Surface Acoustic Waves in Inhomogeneous Media*. Berlin: Springer-Verlag, 1995, pp. 255-259.

[118] I. M. Mason, J. Chambers, and P. E. Lagasse, "Laser-probe analysis of field distributions within acoustic-surface-wave planar resonators", *Electron. Lett.* **11**, pp. 288–290 (1975).

[119] E. J. Staples and R. C. Smythe, "Surface acoustic wave resonators on ST-quartz", in *Proc. IEEE Ultrasonics Symposium*, pp. 307–310 (1975).

[120] J. Schoenwald, "Optical waveguide model for SAW resonators", in *Proc. IEEE Int. Freq. Contr. Symp.*, pp. 340–345 (1976).

[121] H. A. Haus, "Modes in SAW grating resonators", *J. Appl. Phys.* **48**, pp. 4955–4961 (1977).

[122] H. A. Haus and K. L. Wang, "Modes of grating waveguide", *J. Appl. Phys* **49**, pp. 1061–1069 (1978).

[123] L. A. Coldren, H. A. Haus, and K. L. Wang, "Experimental verification of mode shape in s.a.w. grating resonators", *Electron. Lett.* **13**, pp. 642–644 (1977).

[124] G. Clark, R.-F. Milsom, and J. Schofield, "3-D modal analysis of SAW filters", in *Proc. IEEE Ultrasonics Symposium*, pp. 26–31 (1985).

[125] C. K. Campbell, "Modelling the transverse-mode response of a two-port SAW resonator", *IEEE Trans. Ultrason., Ferroelect., Freq. Contr.* **38**, pp. 237–242 (1991).

[126] C. K. Campbell, P. J. Edmonson, and P. M. Smith, "Transverse modes in one-port SAW resonator", *IEEE Trans. Ultrason., Ferroelect., Freq. Contr.* **39**, pp. 785–787 (1992).

[127] O. Männer, G. Scholl, K. C. Wagner, and W. Ruile, "Signal flow graph analysis of transverse modes in a two-port SAW resonator", in *Proc. IEEE Ultrasonics Symposium*, pp. 189–193 (1993).

[128] J. G. Gualtieri and J. A. Kosinski, "Large-area, real-time imaging system for surface acoustic wave devices", *IEEE Trans. Instrum. Meas.* **45**, pp. 872–878 (1996).

[129] W. J. Tanski and H. van de Vaart, "The design of SAW resonators on quartz with emphasis on two ports", in *Proc. IEEE Ultrasonics Symposium*, pp. 260–265 (1976).

[130] S. A. Wilkus, C. S. Hartmann, and R. J. Kansy, "Transverse mode compensation of surface acoustic wave filters", in *Proc. IEEE Ultrasonics Symposium*, pp. 43–47 (1985).

[131] G. Martin, B. Wall, and M. Waihnacht, "An alternative method for suppressing undesired transverse modes in longitudinally coupled SAW resonator filters", *IEEE Trans. Ultrason., Ferroelect., Freq. Contr.* **42**, pp. 1099–1101 (1995).

[132] M. Takeuchi and K. Yamanouchi, "Self-suppression effects of spurious transverse modes in SAW reflectors and resonators with a positive and negative reflectivity", in *Proc. IEEE Ultrasonics Symposium*, pp. 266–269 (1985).

[133] Y. Yamamoto and S. Yoshimoto, "SAW transversely guided mode spurious elimination by optimization of conversion efficiency using W/W0 electrode structure", in *Proc. IEEE Ultrasonics Symposium*, pp. 229–234 (1998).

[134] T. Omori, N. Yokoyama, K. Matsuda, K. Hashimoto, and M. Yamaguchi, "Suppression of transverse mode responses for ultra-wideband and low-loss SAW filters on a Cu-grating/15 °YX-LiNbO$_3$ structure", in *Proc. IEEE Ultrasonics Symposium*, pp. 1056–1060 (2005).

[135] T. Omori, K. Matsuda, N. Yokoyama, K. Hashimoto, and M. Yamaguchi, "Suppression of transverse mode responses in ultra-wideband SAW resonators fabricated on a Cu-grating/15 °YX-LiNbO$_3$ structure", *IEEE Trans. Ultrason., Ferroelect., Freq. Contr.* **54**, pp. 1943–1948 (2007).

[136] M. Mayer, A. Bergmann, G. Kovacs, and K. Wagner, "Low loss recursive filters for basestation applications without spurious modes", in *Proc. IEEE Ultrasonics Symposium*, pp. 1061–1064 (2005).

[137] J. Koskela, J. V. Knuuttila, T. Makkonen, V. P. Plessky, and M. M. Salomaa, "Acoustic loss mechanisms in leaky SAW resonators on lithium tantalate", in *Proc. IEEE Ultrasonics Symposium*, pp. 209–213 (2000).

[138] V. P. Plessky and J. Koskela, "Coupling-of-modes analysis of SAW devices", *Int. J. High Speed El. and Syst.* **10**, pp. 867–947 (2000).

[139] R. M. Finne and D. L. Klein, "A water-amine-complexing agent system for etching silicon", *J. Electrochem. Soc.: Solid State Science* **114**, pp. 965–970 (1967).

[140] O. N. Tufte, P. W. Chapman, and D. Long, "Silicon diffused-element piezoresistive diaphragms", *J. Appl. Phys.* **33**, pp. 3322–3327 (1962).

[141] L. M. Roylance and J. B. Angell, "A batch-fabricated silicon accelerometer", *IEEE Trans. Electron Devices* **26**, pp. 1911–1917 (1979).

[142] F. Goodenough, "Airbags boom when IC accelerometer sees 50 g", *Electron. Des.* **39**, pp. 45–56 (1991).

[143] P. F. V. Kessel, L. J. Hornbeck, R. E. Meier, and M. R. Douglass, "A MEMS-based projection display", *Proc. IEEE* **86**, pp. 1687–1704 (1998).

[144] L. J. Hornbeck, "Frame addressed spatial light modulator", U.S. patent 4,615,595, Oct 1986.

[145] N. Maluf and K. Williams, *An Introduction to Microelectromechanical Systems Engineering*, 2nd ed. Boston: Arctech House, 2004.

[146] G. M. Rebeiz, *RF MEMS: Theory, Design, and Technology*. Hoboken: John Wiley & sons, 2003.

[147] V. K. Varadan, K. J. Vinoy, and K. A. Jose, *RF MEMS and Their Applications*. Chichester: John Wiley & sons, 2003.

[148] S. Lucyszyn, "Review of radio frequency microelectromechanical systems technology", *IEE Proc. Sci. Meas. Technol.* **151**, pp. 93–103 (2004).

[149] K. E. Petersen, "Silicon as a mechanical material", *Proc. IEEE* **70**, pp. 420–457 (1982).

[150] M. Esashi and T. Ono, "From MEMS to nanomachines", *J. Phys. D: Appl. Phys.* **38**, pp. R223–R230 (2005).

[151] H. C. Nathanson and R. A. Wickstrom, "A resonant-gate silicon surface transistor with high-Q band-pass properties", *Appl. Phys. Lett.* **7**, pp. 84–86 (1965).

[152] H. C. Nathanson, W. E. Newell, R. A. Wickstrom, and J. J. R. Davis, "The resonant gate transistor", *IEEE Trans. Electron Devices* **ED-14**, pp. 117–133 (1967).

[153] R. J. Wilfinger, P. H. Bardell, and D. S. Chhabra, "The resonistor: A frequency selective device utilizing the mechanical resonance of a silicon substrate", *IBM J. Res. Develop.* **12**, pp. 113–118 (1968).

[154] C. T.-C. Nguyen, "Frequency-selective MEMS for miniaturized low-power communication devices", *IEEE Trans. Ultrason., Ferroelect., Freq. Contr.* **47**, pp. 1486–1503 (1999).

[155] L. Lin, R. T. Howe, and A. P. Pisano, "Microelectromechanical filters for signal processing", *J. Microelectromechan. Syst.* **7**, pp. 286–294 (1998).

[156] F. D. Bannon III, J. R. Clark, and C. T.-C. Nguyen, "High-Q HF microelectromechanical filters", *IEEE J. Solid-State Circuits* **35**, pp. 512–526 (2000).

[157] Y. Ahn, H. Guckel, and J. D. Zook, "Capacitive microbeam resonator design", *J. Micromech. Microeng.* **11**, pp. 70–80 (2001).

[158] Y. S. Hong, J. H. Lee, and S. H. Kim, "A laterally driven symmetric micro-resonator for gyroscopic applications", *J. Micromech. Microeng.* **10**, pp. 452–458 (2000).

[159] W. C. Tang, T.-C. H. Nguyen, and R. T. Howe, "Laterally driven polysilicon resonant microdevices", *Sensors and Actuators* **20**, pp. 25–32 (1989).

[160] T. Mattila, J. Kiihamäki, T. Lamminmäki, O. Jaakkola, P. Rantakari, A. Oja, H. Seppä, H. Kattelus, and I. Tittonen, "A 12 MHz micromechanical bulk acoustic mode oscillator", *Sensors and Actuators A* **101**, pp. 1–9 (2002).

[161] J. J. Yao and N. C. MacDonald, "A micromachined, single-crystal silicon, tunable resonator", *J. Micromach. Microeng.* **6**, pp. 257–264 (1996).

[162] K. Wang, A.-C. Wong, and C. T.-C. Nguyen, "VHF freefree beam high-Q micromechanical resonators", *J. Microelectromech. Syst.* **9**, pp. 347–360 (2000).

[163] M. U. Demirci and C. T.-C. Nguyen, "Higher-mode free-free beam micromechanical resonators", in *Proc. IEEE Int. Freq. Cont. Symp.*, pp. 810–818 (2003).

[164] V. Kaajakari, T. Mattila, A. Oja, J. Kiihamäki, and H. Seppä, "Square-extensional mode single-crystal silicon micromechanical resonator for low phase noise oscillator applications", *Electron Dev. Lett.* **25**, pp. 173–175 (2004).

[165] O. Holmgren, K. Kokkonen, V. Kaajakari, A. Oja, and J. V. Knuuttila, "Direct optical measurement of the Q values of RF-MEMS resonators", in *Proc. IEEE Ultrasonics Symposium*, pp. 2112–2115 (2005).

[166] D. M. Pozar, *Microwave Engineering*, 2nd ed. New York: John Wiley & Sons, 1998.

[167] R. M. A. Fatah, "Electrostatic activation of micromechanical resonators", *Electron. Lett.* **27**, pp. 166–168 (1991).

[168] A. Bosseboeuf and S. Petitgrand, "Characterization of the static and dynamic behaviour of M(O)EMS by optical techniques: status and trends", *J. Micromech. Microeng.* **13**, pp. S23–S33 (2003).

[169] C. Q. Davis and D. M. Freeman, "Using a light microscope to measure motions with nanometer accuracy", *Opt. Eng.* **37**, pp. 1299–1304 (1998).

[170] B. Serio, J. J. Hunsinger, and B. Cretin, "In-plane measurements of microelectromechanical systems vibrations with nanometer resolution using the correlation of synchronous images", *Rev. Sci. Instrum.* **75**, pp. 3335–3341 (2004).

[171] J. J. Hunsinger and B. Serio, "FPGA implementation of a digital sequential phase-shift stroboscope for in-plane vibration measurements with subpixel accuracy", *IEEE Trans. Instrum. Meas.* **57**, pp. 2005–2011 (2008).

[172] F. Yang, X. He, and C. Quan, "Characterization of dynamic microgyroscopes by use of temporal digital image correlation", *Appl. Opt.* **45** (2006).

[173] D. J. Burns and H. F. Helbig, "A system for automatic electrical and optical characterization of microelectromechanical devices", *J. Microelectromechan. Syst.* **8**, pp. 473–482 (1999).

[174] W. Hemmert, M. S. Mermelstein, and D. M. Freeman, "Nanometer resolution of three-dimensional motions using videointerference microscopy", in *Proc. IEEE MEMS'99*, pp. 302–308 (1999).

[175] S. Petitgrand, R. Yahiaoui, K. Danaie, A. Bosseboeuf, and J. Gilles, "3D measurement of micromechanical devices vibration mode shapes with a stroboscopic interferometric microscope", *Opt. Lasers Eng.* **36**, pp. 77–101 (2001).

[176] M. R. Hart, R. A. Conant, K. Y. Lau, and R. S. Muller, "Stroboscopic interferometer system for dynamic MEMS characterization", *J. Microelectromechan. Syst.* **9**, pp. 409–418 (2000).

[177] J. A. Conway, J. V. Osborn, and J. D. Fowler, "Stroboscopic imaging interferometer for MEMS performance measurement", *J. Microelectromechan. Syst.* **16**, pp. 668–674 (2007).

[178] X. Hu, G. Liu, C. Hu, T. Guo, and X. Hu, "Characterization of static and dynamic microstructures by microscopic interferometry based on a fourier transform method", *Meas. Sci. Technol.* **17**, pp. 1312–1318 (2006).

[179] S. Ellingsrud and O. J. Lokberg, "Analysis of high-frequency vibrations using TV holography", *J. Phys. D: Appl. Phys.* **21**, pp. S11–S13 (1988).

[180] P. Aswendt, C. D. Schmidt, D. Zielke, and S. Schubert, "ESPI solution for non-contacting MEMS-on-wafer testing", *Opt. Lasers Eng.* **40**, pp. 501–515 (2003).

[181] W. M. van Spengen, R. Puers, R. Mertens, and I. De Wolf, "Characterization and failure analysis of MEMS: high resolution optical investigation of small out-of-plane movements and fast vibrations", *Microsyst. Technol.* **10**, pp. 89–96 (2004).

[182] C. Rembe and R. S. Muller, "Measurement system for full three-dimensional motion characterization of MEMS", *J. Microelectromech. Syst.* **11**, pp. 479–488 (2002).

[183] S. Petitgrand and A. Bosseboeuf, "Simultaneous mapping of out-of-plane and in-plane vibrations of MEMS with (sub)nanometer resolution", *J. Micromech. Microeng.* **14**, pp. S97–S101 (2004).

[184] X. Hu, C. Hu, Z. Chen, T. Guo, and X. Hu, "Measuring in-plane and out-of-plane coupled motions of microstructures by stroboscopic microscopic interferometry", *Optics and Laser Technology* **39**, pp. 1176–1182 (2007).

[185] Polytec, polytec home page. (2008). [Online]. Available: http://www.polytec.com/.

[186] J. F. Vignola, X. Liu, S. F. Morse, B. H. Houston, J. A. Bucaro, M. H. Marcus, D. M. Photiadis, and L. Sekaric, "Characterization of silicon micro-oscillators by scanning laser vibrometry", *Rev. Sci. Instrum.* **73**, pp. 3584–3588 (2002).

[187] J. S. Burdess, A. J. Harris, D. Wood, R. J. Pitcher, and D. Glennie, "A system for the dynamic characterization of microstructures", *J. Microelectromechan. Syst.* **6**, pp. 322–328 (1997).

[188] J. L. Blackshire and S. Sathish, "Characterization of MEMS transducer performance using near-field scanning interferometry", *IEEE Trans. Ultrason., Ferroelect., Freq. Contr.* **49**, pp. 669–674 (2002).

[189] P. Sanz, J. Hernando, J. Vázquez, and J. L. Sánchez-Rojas, "Laser vibrometry and impedance characterization of piezoelectric microcantilevers", *J. Micromech. Microeng.* **17**, pp. 931–937 (2007).

[190] C. Rembe and A. Dräbenstedt, "Laser-scanning confocal vibrometer microscope: Theory and experiments", *Rev. Sci. Instrum.* **77**, p. 083702 (2006).

[191] Y. Zhong, G. Zhang, C. Leng, and T. Zhang, "A differential laser Doppler system for one-dimensional in-plane motion measurement of MEMS", *Measurement* **40**, pp. 623–627 (2007).

[192] R. Gutierrez, K. Shcheglov, and T. Tang, "Interferometric system for precision imaging of vibrating structures", Sep 2001, US Patent 6,291,145.

[193] L. A. J. Davis, D. R. Billson, D. A. Hutchins, and R. A. Noble, "Visualizing acoustic displacements of capacitive micromachined transducers using an interferometric microscope", *Acoustics Research Letters Online* **6**, pp. 75–79 (2005).

[194] L. C. Chen, Y. T. Huang, and K. C. Fan, "A dynamic 3-D surface profilometer with nanoscale measurement resolution and MHz bandwidth for MEMS characterization", *IEEE/ASME Trans. Mechatronics* **12**, pp. 299–307 (2007).

[195] L. C. Chen, Y. T. Huang, X. L. Nguyen, J. L. Chen, and C. C. Chang, "Dynamic out-of-plane profilometry for nano-scale full-field characterization of MEMS using stroboscopic interferometry with novel signal deconvolution algorithm", *Opt. Lasers Eng.* **47**, pp. 237–251 (2009).

[196] J. E. Graebner, S. Pau, and P. L. Gammel, "All optical excitation and detection of microelectrical-mechanical systems", *Appl. Phys. Lett.* **81**, pp. 3531–3533 (2002).

[197] A. Caronti, H. Majjad, S. Ballandras, G. Caliano, R. Carotenuto, A. Iula, V. Foglietti, and M. Pappalardo, "Vibration maps of capacitive micromachined ultrasonic transducers by laser interferometry", *IEEE Trans. Ultrason., Ferroelect., Freq. Contr.* **49**, pp. 289–292 (2002).

[198] H. Martinussen, A. Aksnes, and H. E. Engan, "Wide frequency range measurements of absolute phase and amplitude of vibrations in micro- and nanostructures by optical interferometry", *Optics Express* **15**, pp. 11 370–11 384 (2007).

[199] C. Chao, Z. Wang, W. Zhu, and O. Tan, "Scanning homodyne interferometer for characterization of piezoelectric films and microelectromechanical systems devices", *Rev. Sci. Instrum.* **76**, p. 063906 (2005).

[200] V. Annovazzi-Lodi, S. Merlo, and M. Norgia, "Comparison of capacitive and feedback-interferometric measurements on MEMS", *J. Micromech. Microeng.* **10**, pp. 327–335 (2001).

[201] V. Annovazzi-Lodi, S. Merlo, and M. Norgia, "Characterization of silicon microstructures by feedback interferometry", *J. Opt. A: Pure Appl. Opt.* **4**, pp. S311–S317 (2002).

[202] W. T. Pike and I. M. Standley, "Determination of the dynamics of micromachined lateral suspensions in the scanning electron microscope", *J. Micromech. Microeng.* **15**, pp. S82–S88 (2005).

[203] C. L. Wong and W. K. Wong, "In-plane motion characterization of MEMS resonators using stroboscopic scanning electron microscopy", *Sensors and Actuators A* **138**, pp. 167–178 (2007).

[204] B. Ilic, S. Krylov, L. M. Bellan, and H. G. Craighead, "Dynamic characterization of nanoelectromechanical oscillators by atomic force microscopy", *J. Appl. Phys.* **101**, p. 044308 (2007).

[205] A. San Paulo, J. P. Black, R. M. White, and J. Bokor, "Detection of nanomechanical vibrations by dynamic force microscopy in higher cantilever eigenmodes", *Appl. Phys. Lett.* **91**, p. 053116 (2007).

[206] S. Basrour, H. Majjad, J. R. Coudevylle, and M. de Labachelerie, "Simulation and characterization of high Q microresonators fabricated by UV LIGA", in *Technical Proceedings of the 2001 International Conference on Modeling and Simulation of Microsystems*, pp. 294–297 (2001).

[207] Saleh and Teich, *Fundamentals of Photonics.* John Wiley & sons, 1991.